Gastruloid patterning reflects division of labor among biased stem cell clones

Vinay Ayyappan[1], Catherine G Triandafillou[1], Kavitha Sarma[2, 3], Arjun Raj[1, 4, *]

[1]Department of Bioengineering, School of Engineering and Applied Sciences, University of Pennsylvania, Philadelphia, PA, USA
[2]The Wistar Institute, Gene Expression and Regulation Program, Philadelphia, PA, USA.
[3]Department of Cell and Developmental Biology, Perelman School of Medicine, University of Pennsylvania, Philadelphia, PA, USA.
[4]Department of Genetics, Perelman School of Medicine, University of Pennsylvania, Philadelphia, PA, USA.
*Correspondence: arjunrajlab@gmail.com

Abstract

Embryonic development typically requires precise coordination among cells to achieve reproducible outcomes, leading to the assumption that cellular heterogeneity must be minimized or buffered against. Using fluorescence-based lineage tracing in combination with spatial transcriptomics, we show that, in the gastruloid model of early development, pre-existing heterogeneity promotes proper axial organization through division of labor among stem cell clones. Individual clones isolated from a common population exhibit consistent spatial propensities for anterior or posterior fates. While pure clones generate elongated structures less frequently than a polyclonal population, mixing clones restores proper axial elongation. Spatial transcriptomics reveals that pure clones show disrupted gene expression with inappropriate coexpression of anterior and posterior markers, while clone combinations restore proper spatial organization. Using RNA-seq, ATAC-seq, and perturbations to key developmental signaling pathways, we further profile differences among clones and suggest a model whereby developmental precision emerges from the coordinated action of intrinsically biased clonal populations.

Introduction

Embryonic development is a highly coordinated process in which initially similar cells rapidly diversify in fate and structure to form the complex, stereotyped tissues of the mature organism. Developmental outcomes are typically reproducible and precise[1]; thus, any variability in gene expression, signaling, or cell behavior has generally been viewed as noise that has to be buffered against[2–7]. Recent work, however, has indicated that some degree of variability in development might enable flexibility in the face of environmental perturbations[8–12]. Therefore, could intrinsic diversity within an embryonic stem cell population actually *enable* robust patterning and symmetry breaking? In other words, might cellular heterogeneity not hinder, but facilitate, the reproducible self-organization of complex structures, and if so, how?

The gastruloid is a model of early development that is well-suited for testing whether heterogeneity among cells benefits or impedes morphogenesis[13,14]. Gastruloids begin as 3D aggregates of embryonic stem cells (ES cells) that break symmetry in response to a uniformly administered Wnt agonist and elongate. Even in the absence of maternal cues or predefined patterning centers, gastruloids self-organize to spontaneously produce cell types derived from all three germ layers, organized along the anterior-posterior (A-P) body axis.

A fundamental question is whether cellular heterogeneity helps or hinders cellular function in the multicellular context, in particular, cells' capacity to self-organize. The ES cells used to form gastruloids are typically assumed to be functionally equivalent, with heterogeneity between cells treated as stochastic noise[15,16]. However, multiple studies[17–19] have revealed that, even under carefully controlled culture conditions, ES cells frequently fluctuate in state, with expression of pluripotency genes and lineage markers changing in time[20,21]. The question is whether these fluctuations have any functional consequences for development. The assumption has generally been that communication between cells may diminish the downstream

consequences of such variability, thereby homogenizing cell behaviors to promote consistent developmental progression[22–26]. However, an alternative view is that cell-cell variability at early stages may actively promote consistent developmental outcomes rather than undermining them.

One possible way in which developing systems could benefit from cellular heterogeneity is “division of labor,” whereby cells, even of the same type, cooperate by adopting complementary roles to collectively enhance morphogenesis. This principle is well-established across biological systems: social insects coordinate through specialized castes[27], microbial communities distribute metabolic functions among subpopulations[28], and even cancer cell populations exhibit cooperative division of labor[28,29]. One highly relevant example comes from blastocyst complementation experiments, in which a mutant blastocyst that is unable to form a particular tissue is complemented by adding pluripotent stem cells that are able to form those tissues[30]. Remarkably, those pluripotent stem cells are specifically directed to form those tissues, as has been demonstrated in eye[31,32], pancreas[31], and lung development[33]. Whether such division of labor spontaneously emerges in developmental systems like gastruloids and how division of labor influences morphogenetic outcomes remains unknown.

Here, we show that clonal diversity among mouse ES (mES) cells facilitates consistent gastruloid morphogenesis. Using a multicolor fluorescence-based lineage-tracing system, spatial transcriptomics, and chromatin accessibility profiling, we show that individual clones consistently favor specific positional fates along the A-P axis. When combined, biased clones complement each other’s limitations, allowing gastruloids to robustly polarize and elongate. These findings challenge the prevailing view that stem cells in gastruloids are functionally equivalent, revealing instead that clonal diversity drives rather than disrupts reproducible morphogenesis through coordinated division of labor.

Results

Despite individual biases, mES cell clone diversity promotes gastruloid organization

Gastruloids are typically generated from polyclonal mouse embryonic stem cell (mES cell) aggregates. These cells, while often assumed to be homogeneous, can have highly variable states, even under carefully controlled culture conditions[34–39]. Gastruloids, therefore, provide a rich system for mapping the potentially variable characteristics of individual mES cells to their fate outcomes in a self-organizing cellular community. As per the standard mouse gastruloid protocol, we seeded ~300 mES cells in non-adherent conditions (t=0) and applied a timed pulse of Wnt agonist (Chiron, CHIR99021) at 48 hours post-aggregation (t=48). Chiron was removed after 24 hours (t=72), and gastruloids were grown to 120 hours, at which time they should have elongated along a single anterior-posterior (A-P) axis **(Figure 1A)**[1,40–43].

How does variability in the initial mES cell aggregate affect how efficiently gastruloids elongate? We tested the effects of variability by using single-cell-derived clones of mES cells. By deriving a population from a single cell, it is assumed that much of the epigenetic variation in the original population is lost, leading to a population that is more homogeneous than the original bulk population. We asked whether these clonal populations formed gastruloids more or less efficiently than the original bulk population. After isolating individual mESCs by dilution cloning (**Figure 1A**), we compared gastruloids generated from seven individual clonal lines to those from bulk populations, classifying 120-hour gastruloid morphologies into three categories: "elongated" (single A-P axis), "multiaxial" (multiple axes or projections), and "no axis." Each clone could form gastruloids, indicating that they could differentiate into anterior and posterior cell types. Gastruloids generated from bulk mES cells formed elongated gastruloids approximately 75% of the time, in keeping with literature[42]. Gastruloids generated from pure mES cell clones, however, formed elongated structures less frequently, rather forming multiaxial gastruloids or failing to develop a clear axis (3-17 batches, n=8-32 gastruloids per batch; **Figure 1B**). Most clones were thus less efficient than the heterogeneous bulk population at producing properly organized

structures, suggesting these cell populations were more sensitive to initial conditions and thus less robust at gastruloid formation.

The reduced efficiency of pure clones compared to bulk populations suggested that heterogeneity might be beneficial rather than detrimental for gastruloid organization. We hypothesized that heterogeneity in the initial population leads to distinct behaviors among different clones within the bulk population as they organize spatially. To track the behavior of individual clones in a polyclonal aggregate, we implemented a fluorescence-based lineage-tracing strategy whereby mES cells express varying combinations of three fluorophores (mKate2, mOrange2, eGFP) that localize exclusively to the nucleus (**Figure 1A**). We could thereby visually observe how they pattern within gastruloids as they self-organize.

In generating gastruloids from a polyclonal, multicolor population, we observed that cells from the same clone tended to localize to similar regions in the gastruloid (**Supplemental Figure 1**, **Supplemental Movie 1**). Perhaps each clone is biased, such that its cells' fates are skewed to a particular outcome. We generated chimeric aggregates, where 50% (~150 cells) of the starting aggregate was obtained from an unlabeled, bulk mES cell population and the remaining 50% of cells belonged to a single labeled clone. If the clones were unbiased, we might expect labeled cells to be either scattered throughout the gastruloid or to appear in clumps as labeled cells proliferate during gastruloid development. Instead, we noticed that labeled cells in chimeric gastruloids separated from unlabeled bulk ES cells (**Supplemental Movie 2**); that is, the clone seemed to have different sorting properties from the remaining population.

Was spatial separation of labeled clones from the unlabeled bulk mES cells the result of differential adhesion between clone cells and bulk cells or an inherent tendency to form specific tissues in the gastruloid? If differential adhesion were the explanation, we might expect that, across aggregates, fluorescently labeled clones would segregate from their unlabeled counterparts, but for any given clone, labeled cells in some gastruloids would appear in the gastruloid posterior and those in other gastruloids might occupy the anterior. However, we noticed that in the resulting chimeric gastruloids, cells from the labeled clone consistently tended to appear toward either the gastruloid anterior (3 clones) or posterior (2 clones). Each clone had a specific propensity for anterior or posterior domains (Clones 2 and 4 were excluded for technical reasons, see **Methods**), with nearly every gastruloid across several batches of aggregation showing the same pattern for a given labeled clone when combined with unlabeled bulk mES cells (**Figure 1C**, **Supplemental Figure 2A-C**).

These results indicate that clones have specific propensities for the gastruloid anterior or posterior when aggregated with bulk mES cells. We wondered whether clones also demonstrated the same propensities when aggregated in pairs. Aggregates including an "anterior" clone and "posterior" clone resulted in gastruloids with the "anterior" clone occupying the gastruloid anterior and the "posterior" clone occupying the gastruloid posterior (**Figure 1E, Supplemental Figure 2D**). Meanwhile, pairing two "anterior" clones still resulted in relative sorting between the clones, though they appeared slightly more mixed than pairings of clones of opposite propensity. Thus, each clone seemed to display fate biases resulting in spatial propensities during gastruloid morphogenesis, and these fate biases appear to be a property that varies continuously among clones.

While individual clones inefficiently generated elongated gastruloids, we hypothesized that combining the cells of the clone with those from the bulk parental population or even with other clones with different propensities in a chimeric aggregate might improve morphogenesis by allowing each clone to specialize in distinct developmental roles, such as cardiac mesoderm in the anterior and tailbud mesoderm[44] and neuromesodermal progenitors[41,44,45] in the posterior. The principle is that of "division of labor": distinct clones contribute to different tissues or lineages within the gastruloid for which they are better-suited, such that when combined, they can collectively organize more accurately than any individual clone could achieve alone. When we mixed cells from individual clones with bulk cells, the resulting gastruloids had elongated morphologies much more frequently

than gastruloids formed from the pure clone alone. We found that as the percentage of bulk cells in the starting aggregate increased, the proportion of elongated gastruloids increased as well (**Figure 1D**). Even in pure clones (e.g., clone 4) that, alone, rarely formed elongated gastruloids, 50%/50% clone-bulk aggregates formed elongated gastruloids as frequently as bulk mES cell aggregates. To check whether clones that less efficiently formed elongated gastruloids were not being eliminated (e.g., due to competition) from chimeric aggregates, we confirmed that both clones were present in clone-clone and clone-bulk combinations by detecting fluorescence corresponding to cells from either clone (**Supplemental Figure 2F**). Even in clone 4, which rarely formed elongated gastruloids on its own, we saw fluorescent cells from clone 4 in gastruloids where clone 4 comprised 25% of the cells in the initial aggregate, indicating that cells from clone 4 were not completely eliminated during gastruloid elongation. Therefore, introducing heterogeneity to aggregates by combining clones with bulk mES cells improved gastruloids' ability to form elongated structures.

Gastruloids generated from combinations of clones also tended to more consistently form properly elongated structures than pure clones (**Supplemental Figure 2E, Supplemental Figure 3**). Most clone combinations resulted in elongated gastruloids, regardless of whether clones in the chimera were both anterior, both posterior, or if one clone was anterior and the other was posterior. One exception was the combination of clone 4 (likely posterior, see **Methods, Supplemental Figure 2F**) and clone 6 (posterior), which only infrequently (~20%) resulted in elongated gastruloids. On its own, clone 4 formed elongated gastruloids <10% of the time, while clone 6 formed gastruloids that elongated ~50% of the time (**Supplemental Figure 3**). A more heterogeneous mES cell pool in chimeric aggregates thus generally compensates for pure clones' inefficiencies in producing elongated gastruloids, though there are still some clone combinations that do not improve gastruloid morphology over their respective pure clones.

Taken together, these results suggest that although individual mES cell clones might harbor specific spatial propensities and constraints in their ability to generate gastruloids, heterogeneous aggregates can be more capable of properly breaking symmetry to form an elongated gastruloid.

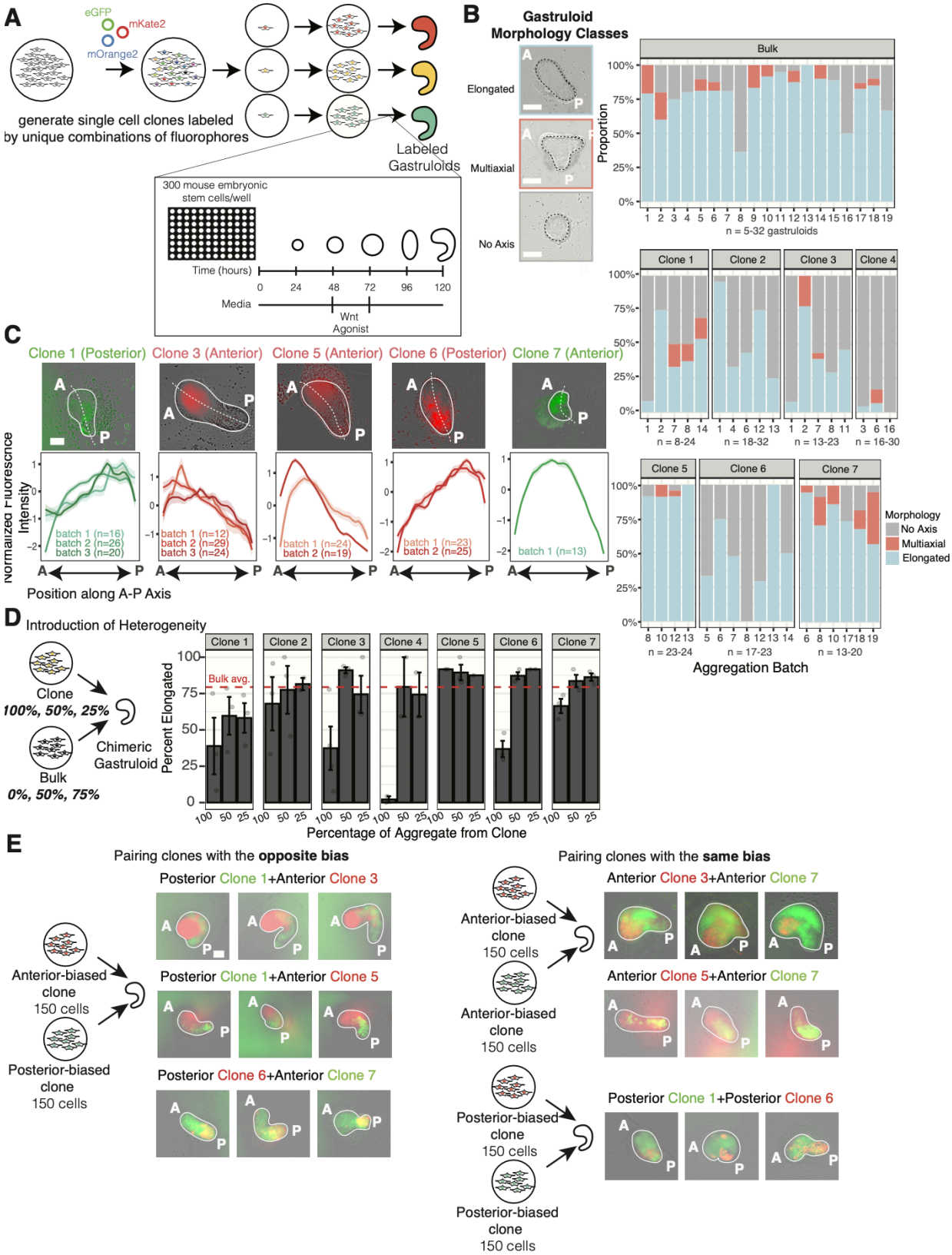

Figure 1. mES cell clone diversity promotes gastruloid self-organization. **(A)**. Schematic describing gastruloid formation and our fluorescent lineage tracing scheme. mES cells expressing unique combinations of the fluorophores eGFP, mKate2, and mOrange2 are dilution cloned and expanded into clonal mES cell lines, which are then used to generate gastruloids. **(B)** Gastruloid morphologies are classified as “elongated,” “multiaxial,” or “no axis”. Bargraphs represent the proportion of gastruloids within each batch of aggregation classified as belonging to a given class of morphologies (n=8-33 gastruloids per batch). The scale bar represents 100px. Annotations (A) and (P) label the gastruloid anterior and posterior, respectively. Each experiment was assigned an “aggregation batch number.” Experiments presented in this panel included pure clone gastruloids and bulk gastruloids; gastruloids aggregated on the same day

share a batch number to enable comparison of pure clone morphologies to bulk gastruloids from the same day/plate. **(C)** Representative Incucyte images of clone-bulk combinations are shown, alongside line graphs showing the normalized (as described in **Methods**) fluorescence intensity along the gastruloid A-P axis. Bold lines show the average intensity profile for gastruloids within a given batch, and error ribbons represent one standard deviation. The scale bar represents 100px. **(D)** 300-cell chimeric aggregates where 100%, 50%, or 25% of the cells belong to a given clone and the remainder of the cells belong to the bulk were generated. Bargraphs showing the average fraction of gastruloids that are "elongated" for each chimeric combination are shown. A dotted red line depicts the average fraction of gastruloids that are "elongated" across aggregation batches. **(E)** Three representative images for each combination of clones. Shown are pairings of anterior-biased clones with posterior-biased clones, anterior-biased clones with anterior-biased clones, and posterior-biased clones with posterior-biased clones. The scale bar represents 100px.

Gastruloids regulate clone proportions

We have shown that individual clones have propensities for certain regions along the A-P axis. We thus wondered about the mechanism: does the spatial organization of clones arise from clones simply redistributing based on their propensities, or does the gastruloid actively adjust clones' proportions within the gastruloid? If clones simply arranged themselves along the A-P axis based on propensity, we would expect each clone to occupy a spatial domain proportional to its initial fractional composition within the aggregate. In contrast, if the gastruloid selectively modulates the growth rates of particular clones to achieve an appropriate final balance based on propensity, then regardless of their starting numbers and ratios, we would expect consistent proportioning of clones along the A-P axis, with clones that are functionally better suited for specific regions expanding preferentially to fill those roles.

To discriminate between these possibilities, we generated aggregates comprising clone 1 (green, posterior propensity) and clone 3 (red, anterior propensity) in ratios of 1:4, 1:2, 1:1, 1:2, and 1:4. We measured fluorescence intensity in red and green channels along the A-P axis of the resulting gastruloids. We found that regardless of the aggregate's starting composition, curves corresponding to each channel's intensity along the A-P axis intersected at ~35% of the distance along the gastruloid A-P axis (**Supplemental Figure 4**). There was batch-to-batch variation in where the intersection point lay; however, the intersection point was not sensitive to the ratio of clone 1 to clone 3 in the initial aggregate (**Supplemental Figure 5**). Thus, when a clone started at high abundance, it grew proportionally less; when it started at low abundance, it compensated by growing more. This constant final proportionality demonstrates active regulation of clones' proliferation by the collective need of the gastruloid rather than competition driven by intrinsic differences in clones' capacity for growth.

We also wondered whether communication between cells before aggregation would affect the propensity of the different clones. To test this possibility, we performed co-culture experiments in which we grew clones 1 and 3 together in a 1:1 ratio for 48 hours before aggregating them. By the time of aggregation, clone 1 accounted for the majority of cells prior to aggregation (**Supplemental Figure 5B)**. Under these conditions, in all resulting gastruloids, clone 3 occupied the anterior and clone 1 occupied the posterior, with average fluorescence intensity profiles intersecting at ~50% of the distance along the A-P axis (**Supplemental Figure 5B, C**). These result show that communication before aggregation did not affect propensity or compensation.

While the above results provide evidence that clones can specialize to form the gastruloid anterior or posterior, we were still left with the question of whether each clone was still capable of establishing both anterior and posterior regions. We performed immunofluorescence staining for the posterior marker T and manually annotated gastruloid outlines and T-expressing regions. Gastruloids generated from pure clones 1 and 6, which each have posterior propensities, had a larger T-positive region on average (~40% of the gastruloid area) than bulk gastruloids (~20% of gastruloids' area) and those made from clones 3, 5, and 7, which have anterior propensity. However, each clone could generate gastruloids containing cells expressing T as well as cells that do not express T (**Supplemental Figure 6A**, **B**). Therefore, each clone, despite exhibiting spatial specialization, is broadly capable of establishing both anterior and posterior identities.

Spatial transcriptomics reveals disrupted spatial segregation of marker genes in pure-clone gastruloids

How do spatial gene expression features of pure-clone gastruloids compare to gastruloids made from bulk mESCs? Since gastruloids formed from pure clones so often fail to elongate or properly polarize, one possibility is that spatial propensities of an individual clone disrupt the establishment of positional identities. Such disruption may manifest as inappropriate expression or coexpression of anterior and posterior markers in the posterior or anterior region, respectively. We used spatial transcriptomics to directly examine spatial gene expression patterns in pure-clone versus bulk gastruloids. We used a panel of 21 genes, comprising marker genes for cell types expected to be in the gastruloid at 120 hours, to perform sequential single-molecule RNA FISH (seqFISH)[46] (**Figure 2A**). We tested gastruloids from a bulk mES cell population (n=2), posterior clone 1 (n=5), anterior clone 3 (n=5), and posterior clone 6 (n=2).

To test whether pure-clone gastruloids fail to properly form and organize cells into anterior and posterior identities, we first examined the spatial relationship between T, a marker of the gastruloid posterior, and Igfbp5, an anterior marker. In well-organized gastruloids, we expect these markers to be spatially segregated and mutually exclusive, reflecting proper patterning along the anterior-posterior axis. Gastruloids generated from a bulk mES cell population had polarized expression of *T*, which was mutually exclusive with expression of *Igfbp5*. However, gastruloids generated from a pure clone, which were less capable of forming elongated structures, had visible patches of *T* and *Igfbp5* that were often intermixed, with some cells coexpressing the two genes (**Figure 2B**, **Supplemental Figure 7A**). Of note, bulk gastruloids had strong expression of *Igfbp5* and *T* in the right locations. Clone 3 gastruloids (anterior propensity) had expression of *Igfbp5* and *T* similar to bulk (**Supplemental Figure 7D**). In contrast, clone 6 gastruloids (posterior propensity) had low overall expression of *Igfbp5* but still had strong expression of posterior markers like *T* and *Cyp26a1* (another posterior marker), consistent with its propensity.

To quantify differences in the spatial organization of marker gene expression, we first used the Moran's I statistic to determine whether gene expression patterns are clustered (cells with similar gene expression are near one another, corresponding to a positive Moran's I), spatially dispersed (i.e., cells with high gene expression must be surrounded by cells with low gene expression and vice versa, corresponding to a negative Moran's I), or random (zero). In general, Moran's I values for genes in our panel were higher for the bulk gastruloids than for gastruloids generated from a pure clone, indicating more spatially clustered gene expression in bulk gastruloids (**Figure 2C**, **Supplemental Figure 7B**). Even in an example of a bulk gastruloid that was not properly elongated, markers like *Igfbp5*, *T*, *Hoxb9*, and *Sox2* were appropriately confined, with relatively high Moran's I values (**Supplemental Figure 8**). Our results were consistent with pure-clone gastruloids doing a poorer job of polarizing marker gene expression.

Next, we wanted to determine whether pure-clone gastruloids coexpressed anterior and posterior marker genes. In general, we expected the expression of these marker genes to be mutually exclusive. A cell with high expression of anterior markers would likely have low expression of posterior markers, and a cell with high expression of posterior markers would have low expression of anterior markers, resulting in an "L-shaped" scatter between the two genes. We devised a metric, which we term the "L-metric," to quantify the degree to which gene expression pairs are mutually exclusive (**Methods**). Negative values indicate mutual exclusivity, positive values indicate coexpression. For example, we expect *T* and *Igfbp5* to have a negative L-metric value, as might *Wnt3* with the Wnt inhibitor *Sfrp1*. Indeed, for these gene pairs that we expect to be mutually exclusive, bulk gastruloids consistently had negative L-metric values (**Figure 2D**, **Supplemental Figure 7C**). Pure-clone gastruloids, on the other hand, had less strongly negative L-metric values. Of the clones tested, clone 1 showed L-metric values most similar to bulk, while clone 6 (posterior propensity) showed positive L-metric values, on average, for *T* and *Igfbp5*, *Cyp26a1,* and *Sfrp1*, and *Wnt3* and *Sfrp1* (**Supplemental**

Figure 7, see **Methods** for statistical comparison of gene mutual exclusivity). Thus, cells from clones with anterior propensity showed more "mixed" expression patterns when forming cells with posterior identities, and cells from clones with posterior propensity showed mixed expression patterns when forming anterior tissues.

Combining clones mitigates disrupted spatial gene expression patterns

Since clone combinations more consistently produced elongated gastruloids, we tested whether chimeric gastruloids showed the coherent spatial gene expression seen in bulk gastruloids. We performed seqFISH on gastruloids generated from a combination of one anterior clone (clone 3) and one posterior clone (clone 1) (n=2) and from a combination of two posterior clones (clone 1 and clone 6) (n=3). Chimeric gastruloids formed from clone pairs now showed more similar Moran's I values to bulk (n=2) for most genes in the panel (**Figure 2E**, **Supplemental Figure 7B**). There were some exceptions; for example, the Moran's I value for the anterior marker *Igfbp5* was much lower than bulk in gastruloids generated from the posterior-posterior combination of clone 1 and clone 6. These gastruloids had robustly polarized *T* expression, but only sparse expression of *Igfbp5*. Thus, combining distinct mES cell clones at least partially restores the spatial gene expression coherence we observed in bulk gastruloids, in contrast to the disrupted patterns seen above in pure-clone gastruloids.

Next, we wondered if these chimeric gastruloids now had less coexpression of marker genes that were normally mutually exclusive. We again quantified these differences using the L-metric as a measure of mutual exclusivity. For marker gene pairs that showed significant coexpression in pure clones (high L-metric; e.g., *Cyp26a1* vs. *Sfrp1*), we found that the L-metric values in the chimeric gastruloids were far lower, indeed, showing no significant differences from bulk (**Figure 2E**). On average across chimeric gastruloids, we observed negative L-metric values for marker gene pairs like *T* and *Igfbp5*, *Cyp26a1* and *Sfrp1*, and *Wnt3* and *Sfrp1.* However, there was substantial variability among gastruloids, with one gastruloid generated from clone 1 and clone 3 showing many cells that coexpressed *T* and *Igfbp5* (**Supplemental Figure 7C**), and the coexpressing cells tended to belong to clone 3 (**Supplemental Figure 9**). Our analysis of marker gene coexpression thus confirmed our above Moran's I findings through a different measure of spatial gene expression coherence: combining clones at least partially restores more organized gene expression patterns compared to pure-clone gastruloids, consistent with their improved morphogenetic outcomes.

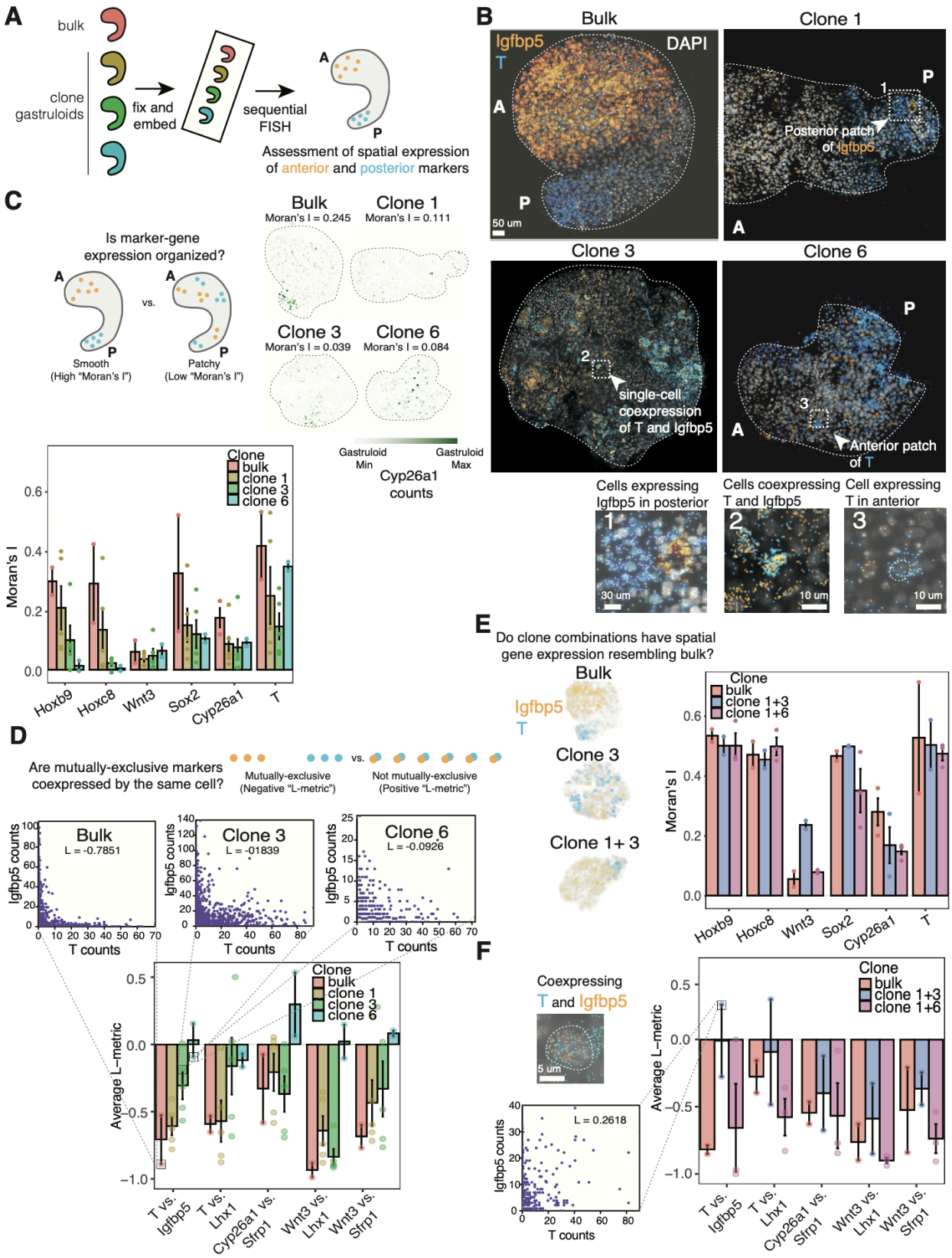

Figure 2. Spatial transcriptomics reveals patterns of gene expression underlying morphologies of pure-clone gastruloids. (A) Schematic describing the experimental workflow. seqFISH was performed on gastruloids made from bulk mES cells and from labeled mES cell clones. **(B)** Representative images showing the expression of *T* (blue) and *Igfbp5* (gold) in gastruloids made from bulk mES cells or mES cell clones 1, 3, and 6. Insets highlight examples where cells are coexpressing *T* and *Igfbp5*, or highlight posterior *Igfbp5* expression or anterior *T* expression. **(C)** Quantification of Moran's I across bulk and pure-clone gastruloids (bulk: n=2, posterior clone 1: n=5, anterior clone 3: n=5, posterior clone 6: n=2) within a batch. Representative gastruloids, where cells are colored on the basis of their *Cyp26a1*, are shown above. **(D)** Quantification of the L-metric across bulk and pure-clone gastruloids within the same batch. Representative hexbin plots are shown, comparing the expression of *T* and *Igfbp5* in selected gastruloids.

(E) Quantification of Moran's I across bulk and chimeric gastruloids from a second seqFISH batch (bulk: n = 2, clone 1+3: n = 2, clone 1+6: n = 3). **(F)** Quantification of L-metric across bulk and chimeric gastruloids from this second seqFISH batch. A representative hexbin plot of *T* and *Igfbp5* expression from a selected clone 1+3 gastruloid is shown, alongside an image of a cell from this gastruloid coexpressing *T* and *Igfbp5*.

Clones can contribute to lineages outside their usual territory

Self-organization involves simultaneous changes in cell type and spatial patterning. Thus, we distinguished between two related but distinct concepts: "fate bias" refers to the intrinsic cellular tendency toward specific lineage outcomes, while "spatial propensity" describes the resulting positional preferences that clones exhibit during gastruloid self-organization, potentially as a result of fate bias. Since gastruloids contain multiple cell types in complex patterns beyond simple anterior-posterior organization, it is possible that spatial propensities might not follow the purely anterior vs. posterior categorization. Along those lines, the division of labor among clones might reflect bias for particular developmental lineages rather than propensity for broad spatial domains; in this case, division of labor might result in cells adopting fates without strict adherence to pure anterior vs. posterior localization.

For example, we looked at localization in chimeric gastruloids generated from clone 1 (posterior propensity) and clone 3 (overall anterior propensity). We found that while overall cells from clone 3 were anteriorly localized and cells from clone 1 were posteriorly localized, some clone 3 cells could be found in the posterior tip of the gastruloid and inappropriately coexpressed anterior marker *Igfbp5* with posterior marker *T*, suggesting they were contributing to some cell types residing in the gastruloid posterior despite their anterior spatial propensity. Further analysis of the expression patterns in these chimeric gastruloids revealed that clone 1 cells, despite their posterior spatial propensity, actually expressed relatively low levels of *T* compared to clone 3 cells, even within the gastruloid posterior, where *T* should be expressed most strongly (**Supplemental Figure 10A**, **B**). That said, clone 1 still had comparatively higher expression of *Thy1*, a marker for posterior neuroectoderm as well as some mesenchymal cell types[45,47,48], confirming its general bias for the posterior. In this particular pairing, clone 3 had a stronger bias for *T*-expressing cell types than clone 1, even though clone 3 typically occupies anterior regions. It is possible that it is thus able to "fill in" for the missing *T*-positive cells based on its propensity.

To determine whether clones occupy regions outside their usual spatial territories in other pairings, we immunostained gastruloids formed from different clone combinations (**Supplemental Figure 10C-E**, **Supplemental Figure 11**) and looked at how much of the area occupied by each clone in a pair was positive for T. In most chimeric gastruloids, a small proportion (typically < 25%) of the anterior clone's area was positive for T. In some specific clone pairings, like clone 1+3 (**Supplemental Figure 10E**, **Supplemental Figure 11**) and clone 6+7 (**Supplemental Figure 11**), the anterior clone occupied the anterior region of the gastruloid, and also had cells residing in the *T*-positive posterior tip of the gastruloid. Division of labor may thus extend beyond anterior-posterior segregation, with clones' biases potentially extending to cell types in addition to broad spatial territories.

Propensity erodes through rounds of passaging

We wondered whether clones' propensities were stable over further rounds of cell division beyond the expansion following isolation (**Supplemental Figure 12**). We generated chimeric gastruloids from pairs of mES cell clones and from pairings of clones with bulk mES cells at multiple passages and found that, though clones had clear propensities at passage 1 post-thaw, aggregates generated at passage 3 were well-mixed. Beyond passage 3, chimeric aggregates, rather than having well-separated clones, frequently developed into gastruloids that featured a mix of labeled clones throughout (**Figure 3A**, **Supplemental Figure 13A-D**). Thus, while clonal propensity was robust to large-scale expansion, it was not preserved through serial passaging after thawing.

We performed replicate experiments with several parental clones across multiple passages. In most cases, clones lost their characteristic propensity by passage 4. However, in some replicate experiments, we observed variability; for example, clone 3 maintained its propensity at passage 4 in a third replicate (**Supplemental Figure 13C**-**D**). These results suggested that propensity is not stably maintained through extended passaging and that loss of propensity may be partially influenced by stochastic or context-dependent factors.

We considered two possibilities for how clones lose spatial propensity during passaging. One possibility is that a small subset of unbiased cells lacking any propensity pre-exist in the population and selectively expand during passaging, overtaking the culture. A second possibility is that individual cells change their propensity during passaging. To distinguish between these scenarios, we performed an additional round of bottlenecking to derive subclones from clonal lines **(Figure 3B)**. We then generated chimeric gastruloids by aggregating each subclone with bulk mES cells. If truly unbiased cells existed within the population, then those unbiased subclones isolated from the parental clone population would mix evenly with bulk mES cells in chimeric gastruloids. Subclones isolated from passage 1 cells of anterior clone 3 and posterior clone 1 retained the spatial propensity of their parent line **(Figure 3C),** and none of the subclones lacked propensity. These results are consistent with the loss of propensity not being due to expansion of an unbiased subpopulation that was already present, although we cannot rule out the possibility that some rare unbiased clones exist in the population. We next passaged the parental clones once and then isolated subclones. Differently then passage 1, subclones isolated from the passage 2 parental clones lacked clear spatial propensities **(Figure 3C)**. This result shows that individual cells change their propensity, reverting to a state with seemingly less propensity. Together, these results suggest that passaging leads to a loss or “forgetting” of the original propensity across the population.

Some post-passage-2 subclones generated gastruloids mostly with a uniform distribution of labeled cells along the A-P axis. Since these subclones tended to uniformly arrange themselves along the gastruloid A-P axis, they likely “lost” their propensity during passaging. Other subclones seemed to feature a mix of propensities, generating some gastruloids with labeled cells predominantly in the anterior and other gastruloids with labeled cells predominantly in the posterior (**Supplemental Figure 14**); some cells within these subclones therefore had anterior propensity and others had posterior propensity. These results suggest that after passaging and over the course of subsequent rounds of cell division, cells within each subclone can acquire anterior or posterior propensities, which may resemble the emergence of diverse propensities within a bulk population.

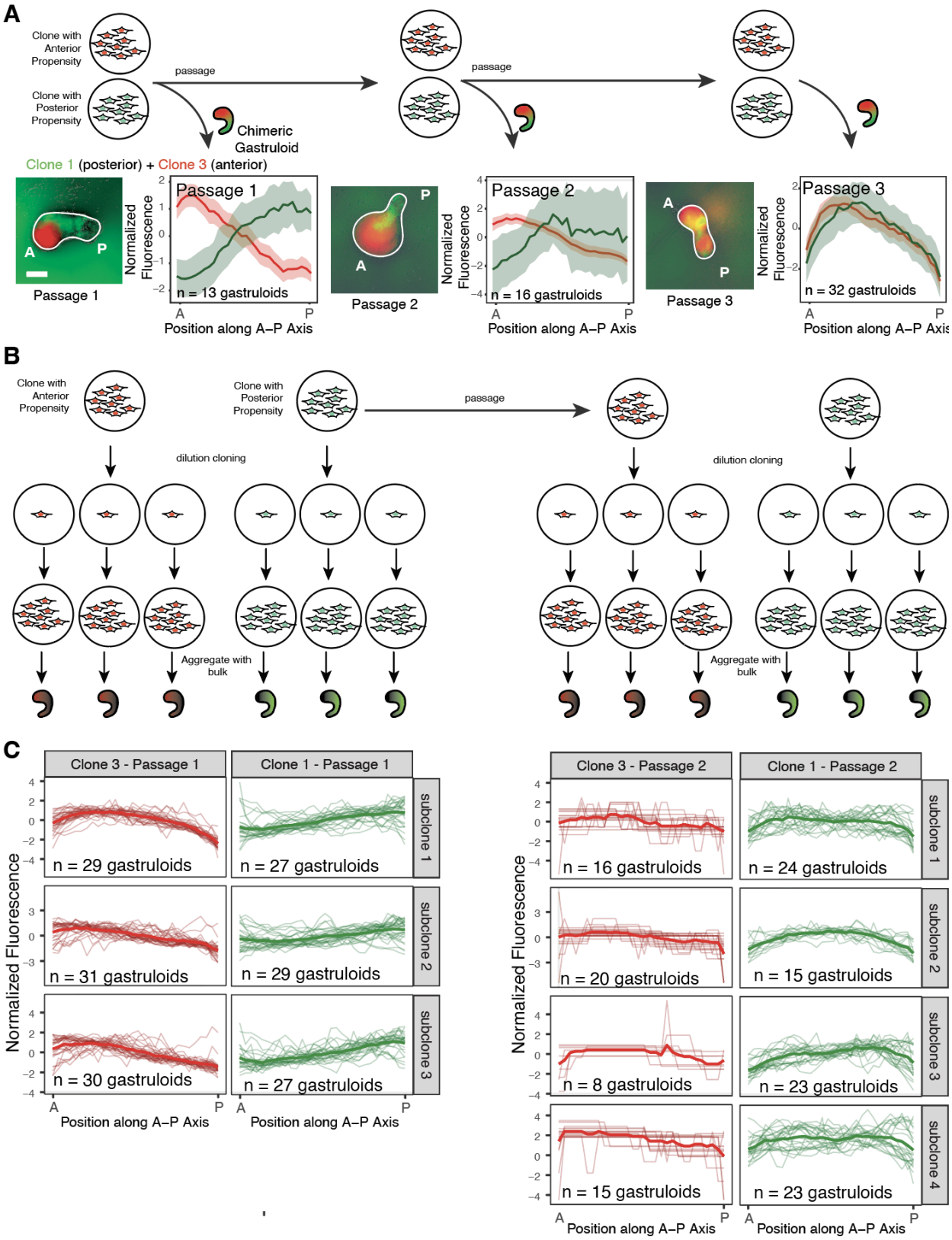

Figure 3. Propensity decreases across passages. **(A)** Representative images and quantification of changes in clones' propensity across three rounds of passaging. Gastruloids from the combination of clone 1 and clone 3 are shown. Scale bars represent 100px. **(B)** Schematic describing isolation of subclones from mES cell clones. **(C)** Individual fluorescence intensity curves for every gastruloid generated from each subclone isolated from clone 1 and clone 3 at passage 1 and at passage 2. Normalization is described in **Methods**.

Propensity is not a consequence of partial differentiation

We wanted to determine what molecular characteristics of clonal mES cells underlie their respective propensities. One possibility is that propensity reflects partially differentiated states of clones. We therefore collected RNA from our clonal mES cell lines (3 anterior clones, 2 posterior clones) and performed bulk RNA-seq to test whether there were transcriptional signatures that correlated with propensity.

We identified 230 differentially expressed genes between anterior and posterior clones out of 14,883 total genes detected (**Figure 4B**). The genes that were differentially expressed showed diverse functions, including cell adhesion (*St8sia6, Nphs1*), chemokine signaling (*Cxcl14*), and growth factor regulation (*Igfbp7*), but did not correspond to coherent developmental pathways or well-known anterior-posterior patterning programs. There were no significant differences in the expression of pluripotency markers (e.g., *Oct4, Sox2, Klf4, Nanog*) (**Figure 4A-C**), nor were there significant differences in expression of markers for cell types present in mature gastruloids (**Figure 4D**), nor in the expression of cadherins (**Supplemental Figure 15A**). The subtle transcriptional differences identified likely reflect heterogeneity in cellular states rather than commitment to specific lineages.

We further tested the differentiation potential of clones by subjecting all to differentiation protocols intended to produce endoderm, mesoderm, or neural cell fates (**Supplemental Figure 16, 17**) and immunostaining for germ layer markers T (mesoderm), Sox17 (endoderm), and Pax6 (neural/ectoderm). Under standard pluripotency conditions, neither clones nor bulk mES cells expressed markers of the germ layers. However, upon directed differentiation, all clones successfully expressed appropriate markers: Sox17 (endoderm), T (mesoderm), and Pax6 (neural/ectoderm). Therefore, clones seem to retain broad differentiation potential and are not partially differentiated toward specific lineages.

Changes in chromatin accessibility at developmentally relevant motifs correlate with propensity

Since propensity did not seem to be associated with coherent expression differences between clones, we wondered if differences in chromatin accessibility were more strongly associated with propensity. Our results showing that propensity diminished over successive passages indicated a form of epigenetic memory that, while not permanent, is stable over many rounds of cell division. We hypothesized that clones with propensities for anterior or posterior fates had epigenetic differences that make drivers of anterior or posterior fates more likely to be expressed. We therefore sought to determine what chromatin accessibility differences exist between mES cell clones differing in propensity. ATAC (assay for transposase-accessible chromatin) sequencing is a way to measure differences in chromatin accessibility. We harvested chromatin from bulk mES cells and mES cells from each clonal line across three rounds of passaging to perform ATAC-seq (**Figure 4A**).

We first focused on differences among clones at passage 1. Were there differences in chromatin accessibility that might indicate differences in priming for anterior or posterior fates among clones (**Figure 4E**-**G)**? Across all samples, we identified 44,540 peaks. The majority of peaks (67.7%) were shared among all clones and bulk mES cells, likely reflecting their common pluripotent identity. However, the remaining peaks we observed were specific to anterior and posterior clones: 3.22% of peaks were unique to anterior clones, while 8.05% were unique to posterior clones. In addition, 3.50% of peaks were unique to bulk, 2.18% were shared between only bulk and posterior clones, 4.01% were shared only between bulk and anterior clones, and 11.24% were shared only between anterior and posterior clones (**Figure 4G**).

In comparing differentially-accessible peaks between clones with anterior and posterior propensities, we observed significant differences in some genomic regions near genes with known functions in development (**Figure 4E**-**G**). For example, posterior clones showed increased accessibility in peaks near *Hes1*, which has a known role in coordinating the timing of differentiation among mES cells in a population[49,50] and in skewing

differentiation toward mesodermal trajectories[50]. We did not find accessibility differences in genomic regions associated with cadherin genes (**Supplemental Figure 15B**).

Next, we also considered later passages, by which time clones had generally lost their visible propensities. We looked at the number of peaks present in anterior clones, posterior clones, or bulk samples. Across all samples, we identified 41,593 peaks, of which 58.5% of peaks were shared among anterior clones, posterior clones, and bulk. 9% of peaks were unique to posterior clones, while <1% of peaks were unique to anterior clones (**Figure 4G**, **Supplemental Figure 18A**, **B**).

What transcription factors might be related to accessibility differences that we observe? At each passage, we used HOMER to identify transcription factor DNA binding motifs enriched among regions differentially-accessible between anterior clones and posterior clones (**Figure 4H**, **Supplemental Figure 18E-G**). At passage 1, we found six motifs significantly enriched in anterior clones compared to posterior clones, including CEBP (a retinoic acid signaling target[51]), Rbpj (a Nodal signaling regulator and Notch target involved in ectoderm-derived tissue differentiation[52,53]), Tcf3 (which inhibits Wnt signaling to promote anterior identity[54,55]), and three Wnt pathway components (TCFL2, Tcf7, LEF1) known to regulate anterior-posterior axis specification[41,56].

The enrichment of CEBP, Rbpj, and Tcf3 in anterior clones is consistent with increased accessibility at regulatory sites for pathways that promote anterior identity–CEBP for retinoic acid-mediated anteriorization, Rbpj for Notch-driven ectoderm specification, and Tcf3 for Wnt pathway repression. The enrichment of Wnt pathway transcription factors in sites of increased chromatin accessibility in anterior clones was initially surprising, since these factors typically promote posterior fates. However, we reasoned that since mES cells were cultured in the presence of Chiron (a Wnt agonist that maintains active Wnt signaling in all cells), anterior clones might have enhanced accessibility at binding sites for Wnt targets involved in negative feedback regulation rather than pathway activation. Consistent with this hypothesis, we observed increased accessibility near Wnt inhibitory genes like *Sp5* and *Fbxw26* in anterior clones[57](**Figure 4E**, **F, Supplemental Figure 18C-D**). RNA-seq analysis revealed 1.57-fold higher expression of the Wnt inhibitor *Axin2* in anterior versus posterior clones (**Supplemental Figure 17C**). These results suggest that anterior clones are primed to more readily activate Wnt pathway inhibitors even under uniform Wnt stimulation, which could explain their propensity for anterior regions during gastruloid development.

While anterior clones showed a reduction in unique peaks, the overall patterns remained similar between passages, suggesting that gross chromatin accessibility differences are maintained even as propensities are lost. The preservation of broad accessibility patterns raises the possibility that the regulatory changes that drive the loss of propensity are specific to particular regulatory pathways. To test this possibility, we checked whether differences in motif enrichment between anterior and posterior clones persisted across passages. We looked at differentially accessible peaks between anterior and posterior clones at passage 2 and passage 3. For motifs enriched in anterior clones at passage 1, we asked what percentage of regions more accessible in anterior clones contained that motif and computed an enrichment score by comparing this percentage to the percentage of randomly selected sequences in the mouse genome that contain that motif using HOMER. Enrichment for all motifs that were enriched in anterior clones at passage 1 decreased progressively in passages 2 and 3 (**Figure 4I)**. The progressive loss of motif enrichment over passages suggests that accessibility differences at developmentally relevant transcription factor binding sites, like Wnt, Nodal, and retinoic acid, underlie clonal propensities.

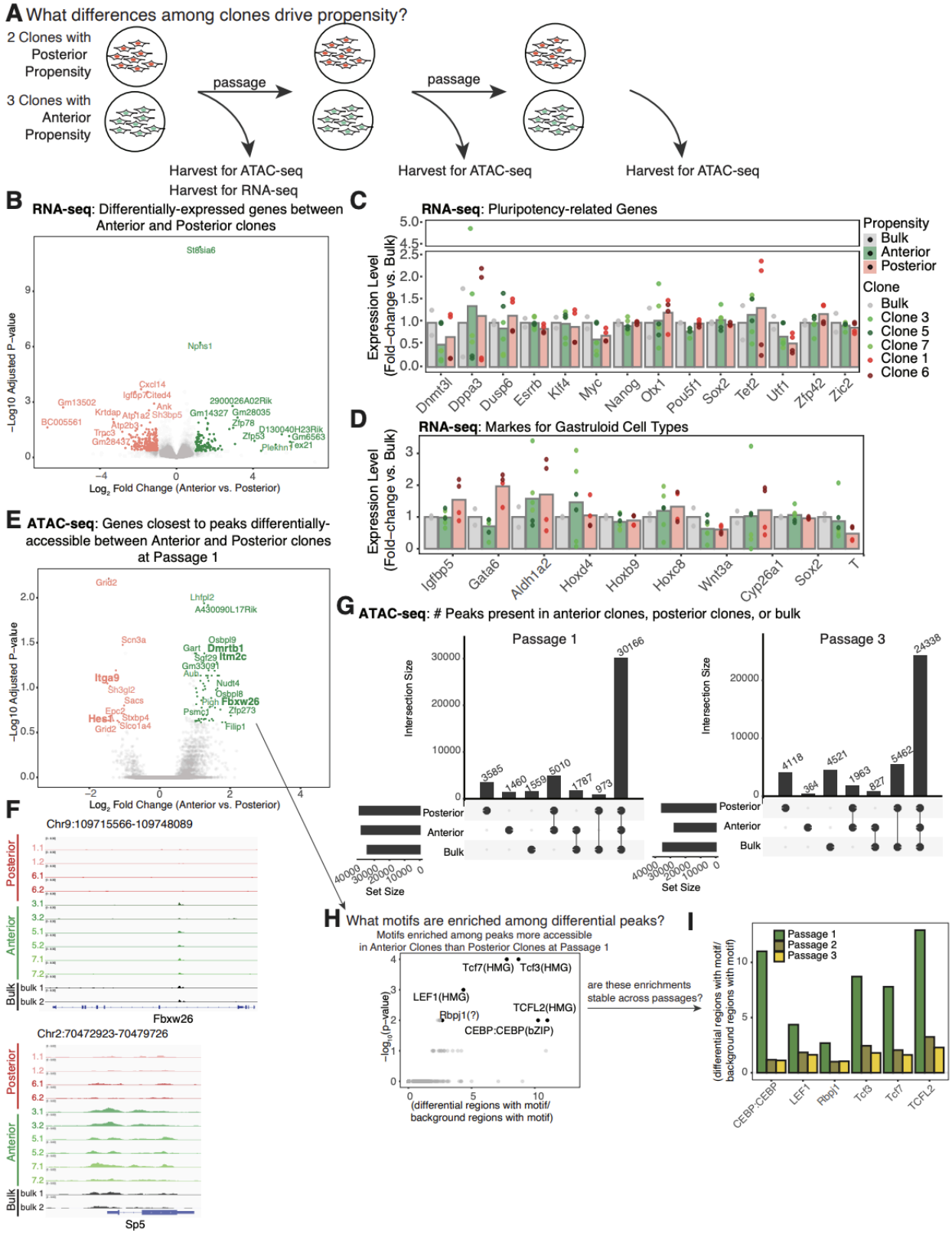

Figure 4. ATAC-seq and RNA-seq of mES cell clones show differences in chromatin accessibility associated with propensity. **(A)** Schematic describing the workflow for harvesting samples for RNA-seq and ATAC-seq. **(B)** Volcano plot showing differentially-expressed genes between anterior clones and posterior clones. **(C)** Bargraph comparing the expression of pluripotency markers among bulk mES cells, anterior clones, and posterior clones. **(D)** Bargraph comparing the expression of marker genes for cell types expected to be present in gastruloids. **(E)** Volcano plot showing genes near differentially-accessible genomic regions between anterior clones and posterior clones. **(F)** Representative ATAC-seq tracks for Fbxw26 and Sp5, genes with genomic regions more accessible in anterior clones. **(G)** Upset plots showing the number of peaks unique to posterior clones, anterior clones, or bulk mESCs or peaks shared among these samples. Plots are shown for samples harvested at passage 1 and at passage 3. **(H)** Scatterplots showing motifs identified by HOMER as being more enriched among peaks more accessible in anterior clones than posterior clones at passage 1. The x-axis shows enrichment scores: the fold-change between the proportion of sequences containing each motif among differentially accessible peaks versus the

proportion of sequences containing each motif among peaks randomly selected through the mouse genome. The y-axis shows adjusted p-values. Labeled peaks have enrichment scores > 2.5 and adjusted p-values < 0.05. **(I)** Barplots comparing motif enrichment scores across passages, for each motif annotated as significant in **(H)**.

Perturbing developmental signaling disrupts propensity

Morphogens, like Wnt, retinoic acid (RA), and Nodal, are thought to shape gastruloid self-organization by forming gradients along which anteroposterior identity is established[58–60]. A cell's position within a gradient thus influences its own fate choice and its ability to modulate the signaling microenvironment for itself and its neighbors. If clones' propensity is shaped by differential responses to morphogen gradients, then perturbing morphogen pathways might distort their arrangement within the gastruloid.

Our ATAC-seq experiments revealed RA and Nodal signaling as plausible pathways associated with propensity. Both pathways are thought to affect the organization of cells in the embryo, in part by modulating their response to Wnt signaling[44,59,60]. We hypothesized that perturbing RA or Nodal signaling should disrupt the characteristic spatial arrangement of clones within gastruloids, either by affecting their ability to segregate from one another or their ability to consistently occupy the gastruloid's anterior or posterior. As above, we defined "propensity" as the tendency of a clone to occupy a specific axial domain, and "sorting" as the spatial segregation of different clones within the gastruloid (**Figure 5A**).

To perturb RA and Nodal signaling, we administered, respectively, 0.15nM RA or 5μM SB-431542 (a disruptor of Activin/Nodal/TGF signaling) after aggregating gastruloids comprising anterior clone 3 and posterior clone 1. We applied perturbations from 96-120 hours after aggregation to minimize effects on initial gastruloid axis establishment and elongation. By 96 hours, *Wnt* signaling has been established and genes like *T* are expressed and polarized, so disrupting developmental signaling pathways should, in principle, have less of an effect on overall gastruloid development than if applied earlier[16,61].

We first wanted to assess the effect of RA treatment or inhibition on propensity. Visually, RA treatment produced a "blended" appearance where clone boundaries became indistinct and cells from both clones were intermixed throughout the gastruloid **(Figure 5B)**. Tracing the fluorescence intensities for red and green channels along the A-P axis of control and treated gastruloids, RA treatment caused average red (clone 3) and green (clone 1) fluorescence intensity profiles to become more similar to one another, suggesting a loss of a difference in propensity between the two clones (**Supplemental Figure 19**). Though gastruloids comprising paired posterior clones 1 and 6 had some degree of mixing at baseline, RA treatment again collapsed the average fluorescence intensity curves for this pairing of clones (**Supplemental Figure 20**). We also tested 100nM AGN-193109, an RA inhibitor, which also resulted in a loss of differential propensity between clone 1 and clone 3 and clone 1 and clone 6 (**Supplemental Figure 21**). Activating or disrupting RA signaling may thus "wash out" differences between clones by either forcing them to a more anterior or posterior fate, respectively, resulting in a loss of differences in propensity between clones in a pair.

Unlike RA treatment, which blended clones throughout the gastruloid, Nodal inhibition preserved clear boundaries between clones. Visually, Nodal inhibition resulted in large, discrete patches where each region was dominated by a single clone, but the patches appeared throughout the A-P axis rather than consistently in anterior or posterior regions (**Figure 5B**). Fluorescence intensity profiles in Nodal-inhibited gastruloids were highly variable (**Figure 5C**), with large peaks in intensity corresponding to each clone's main territories appearing at unpredictable positions along the A-P axis. To quantify the loss of propensity, we measured what fraction of each gastruloid's anterior and posterior regions was occupied by each clone (described in **Methods**). In control gastruloids, clone 3 (anterior propensity) occupied more of the anterior region while clone 1 (posterior propensity) occupied more of the posterior region. However, like RA treatment, Nodal inhibition eliminated preferential localization of either clone to anterior or posterior regions (**Figure 5D**).

We next compared how RA treatment and Nodal inhibition affect clone sorting. We measured the degree of spatial overlap between clones. We generated binary masks from each fluorescent channel, YFP for clone 1 and Cy3 for clone 3, to identify the regions each clone occupied. We then calculated the intersection over union (IOU) between the two masks: the area of overlap divided by the total area covered by either mask. Higher IOU values indicate more overlap between clones, and therefore greater mixing (**Figure 5E-F**, **Supplemental Figure 22**). RA-treated gastruloids showed significantly higher IOU values than both control and Nodal-inhibited gastruloids, consistent with a higher degree of mixing. In contrast, Nodal inhibition had little effect on IOU, indicating that clones remained spatially separated despite a loss of propensity. These results suggest that RA disrupted both propensity and sorting. However, Nodal inhibition primarily disrupted propensity but preserved some degree of sorting, demonstrating that the two processes can be uncoupled.

To determine whether the loss of propensity and sorting we observed was due to specific signaling disruption or a general failure of gastruloids to develop, we examined whether other aspects of gastruloid organization remained intact. Neither RA treatment nor Nodal inhibition significantly increased the frequency of gastruloids lacking an axis or forming multiple axes (**Figure 5G**), indicating that basic morphogenetic processes can proceed even when propensities were lost. seqFISH analysis in SB-431542-treated bulk gastruloids (n = 1) revealed that *T* expression remained polarized, although we observed some coexpression in those *T*-positive cells with the anterior marker *Igfbp5*. Similarly, RA-treated chimeric gastruloids (n = 3) composed of clone 1 and clone 3 (n = 3) could polarize *T* expression but showed coexpression of *T* and *Igfbp5*. We also observed widespread expression of *Sox2*, a gene typically marking posterior identity in our mES cell line[62], suggesting further differences between the RA-treated chimeric gastruloids and untreated gastruloids (**Supplemental Figure 23A-B**). Unlike the gene expression differences observed between clones in control chimeric gastruloids, both RA and Nodal inhibitor treatment reduced gene expression differences between clones (**Supplemental Figure 23C**). Therefore, even in gastruloids that could polarize T and elongate, propensities were disrupted under treatment. Overall, RA and Nodal signaling perturbations disrupted clonal organization while leaving some aspects of axial patterning intact, consistent with a role for morphogen signaling in regulating the spatial behavior of individual clones during gastruloid development.

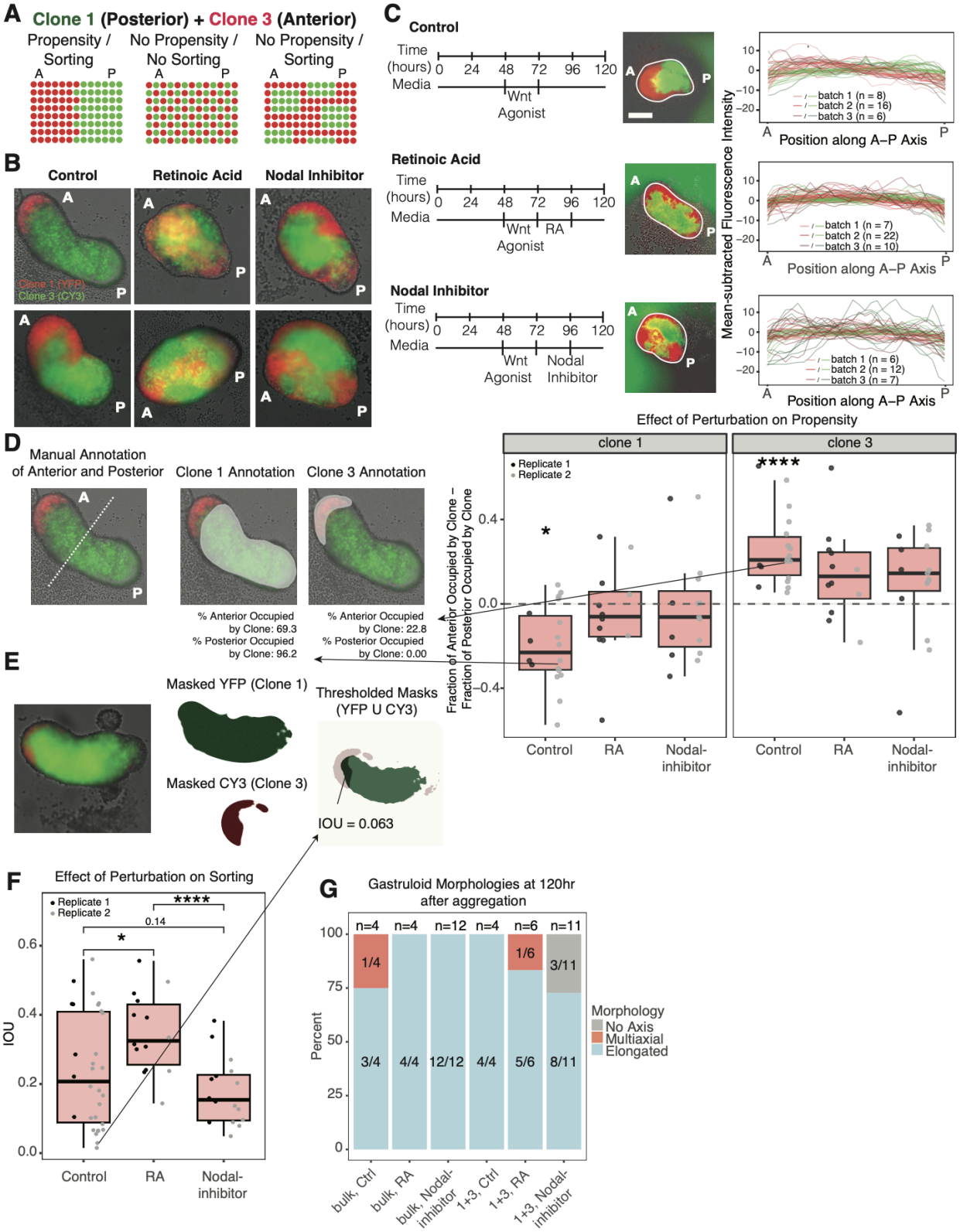

Figure 5. Perturbing Nodal signaling disrupts clones' propensity while maintaining their sorting. **(A)** Schematic describing how cells might sort if they have propensity, how cells might lack propensity and fail to sort, or might sort without having propensity. **(B)** Representative images of gastruloids comprising clone 1 and clone 3 under control conditions, or when treated with retinoic acid or SB431542 (Nodal inhibitor) from 96-120 hours after aggregation. **(C)** Line scans describing the fluorescence intensities in red and green channels along the A-P axis for gastruloids under each condition. Normalization is described in **Methods**. Here, the mean of each line scan was subtracted to enable direct comparison of variation within each condition. Fluorescence intensities in the red channel were scaled to match the range of green fluorescence intensities. Scale bars for corresponding images correspond to 50px. **(D)** Quantification of the effect of chemical perturbation on gastruloid sorting. The fraction of the gastruloid anterior occupied by a given clone, minus the fraction of the gastruloid posterior occupied by that clone, is plotted for clone 1 and clone 3. Asterisks denote statistical significance comparing differences to zero (* p<0.05, ****p<0.0005). **(E)** Workflow for computing IOU. Masks for each channel are shown, along with

composite images displaying masks for both channels (YFP colored in green, Cy3 colored in red). The region of overlap between masks is also shown, along with the IOU for each representative example. **(F)** Boxplots displaying IOU values for gastruloids under each condition. Asterisks denote statistically significant differences between conditions (* $p<0.05$, ****$p<0.0005$). **(G)** Stacked barplots showing the percentage of gastruloids that are elongated, multiaxial, or that have no axis. The plot shows bulk mES cells under control conditions, treated with RA, or treated with Nodal inhibitor and clone 1+3 gastruloids under control conditions, treated with RA, or treated with Nodal inhibitor.

Markers of clonal propensities *in vivo*

We wondered whether the fate biases that influence clones' self-organization in the gastruloid might also exist *in vivo*. Some recent work has identified lineage restriction within the mammalian embryo that arises as early as the epiblast stage[17,63], and we thus sought to determine whether biases in fate outcome manifest in transcriptional signatures that persist through the developmental time course. We analyzed published single-cell RNA-seq data from E12.5 embryos in which epiblast cells had been barcoded (E5.5) and clonally traced through development (**Figure 6A-B**). In this dataset, cells were annotated by tissue type, and we further classified these tissues according to their germ layer of origin. Some barcodes were predominantly found in ectoderm-derived tissues, suggesting that these clones were biased toward ectoderm differentiation (ectoderm propensity). Others showed bias toward mesoderm or endoderm lineages, with correspondingly skewed tissue distributions (ME propensity) (**Supplemental Figure 24A-C**). We asked whether this skew in cell type proportions operates on the basis of principles similar to propensity among clones in the gastruloid. In particular, did clones biased toward or against a given germ layer display gene expression signatures reflective of this bias even at later stages of development?

We first subsetted the dataset to examine gene expression exclusively within barcoded cells belonging to tissues derived from ectoderm (**Figure 6C**). In these ectoderm cells, we asked, do ectoderm cells from clones that produce fewer ectoderm cells (i.e., non-ectoderm propensity) still express markers of other lineages, and do clones biased toward ectoderm (ectoderm propensity) show stronger ectoderm marker expression? We compared the top four clones with the lowest contribution to ectoderm and the top four clones with the highest ectoderm contribution (**Supplemental Figure 24D**). Within ectodermal cells, clones with non-ectoderm propensity showed elevated expression of mesoderm-associated genes. Conversely, clones with ectoderm propensity expressed ectoderm markers such as *Btg2, Hes5, Nes, Nog*, and *Zic2* more strongly. These transcriptional differences persisted despite all analyzed cells being annotated as ectoderm, suggesting that early clonal identity leaves lasting transcriptional signatures that were not fully erased upon lineage commitment, much like the expression patterns we observed in our gastruloid experiments, where clones performing roles misaligned with their propensities showed mixed marker expression.

We next analyzed cells from tissues derived specifically from posterior mesoderm. First, we asked whether clones with propensities to form mesoderm-derived tissues inappropriately express ectodermal genes within posterior mesoderm cells. These effects were subtle because ectoderm-associated genes were expressed at low levels in posterior mesoderm for all the clones (**Figure 6D**). Next, we compared mesoderm marker gene expression between clones with a propensity toward posterior mesoderm (posterior mesoderm propensity) and those with propensities for other tissues. Six out of seven mesoderm markers were more highly expressed in clones with posterior mesoderm propensity, indicating that propensity is reflected in transcriptional signatures even within the same germ layer fate.

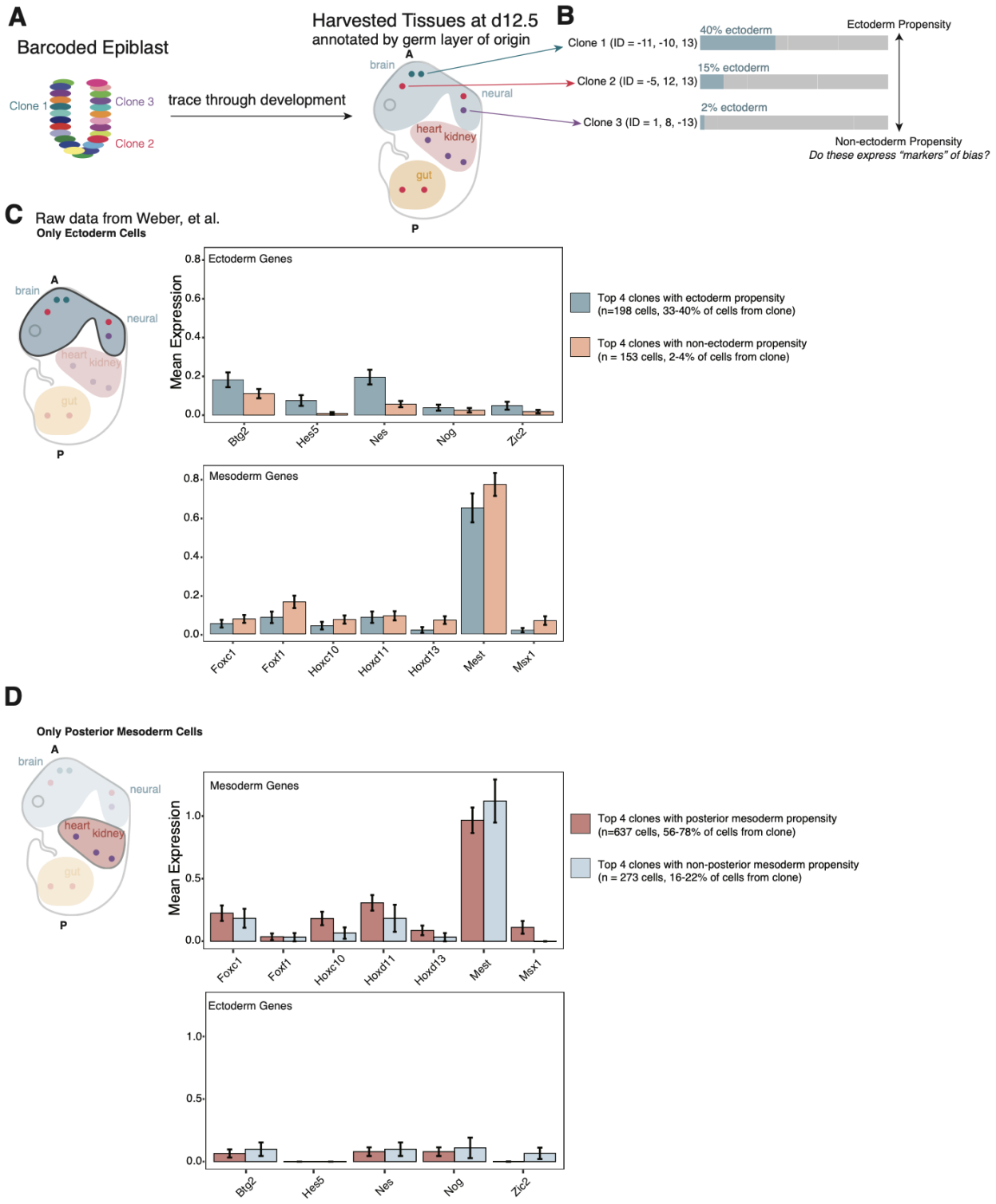

Figure 6. Analysis of an *in vivo* lineage tracing dataset reveals persistent bias through development. (A) Schematic depicting the conceptual workflow. **(B)** The fraction of cells belonging to ectoderm-derived tissues for three clones in the dataset. **(C)** For only cells annotated as belonging to ectoderm, derived tissues, barplots are shown comparing gene expression values for ectoderm markers (*top*) and mesoderm markers *(bottom*), comparing the top 4 clones with the highest proportion of cells in ectoderm tissues and the 4 clones with the lowest proportion of cells in ectoderm tissues. **(D)** For only cells annotated as belonging to posterior mesoderm, derived tissues, barplots are shown comparing gene expression values for mesoderm markers (*top*) and ectoderm markers *(bottom*), comparing the top 4 clones with the highest proportion of cells in posterior mesoderm tissues and the 4 clones with the lowest proportion of cells in posterior mesoderm tissues.

Discussion

Here, we show that heterogeneity among mouse embryonic stem (mES) cells can actively support reproducible self-organization in gastruloids. Traditional gastruloid protocols typically rely on polyclonal mES cell aggregates assumed to be functionally homogeneous. However, we find that even among pluripotent cells of shared origin, individual mES cell clones exhibit consistent spatial propensities in their contributions to gastruloid patterning. This functional diversity is critical for successful axial elongation and tissue organization. Gastruloids formed from single clones rarely elongate properly, whereas mixed aggregates composed of bulk populations or defined pairs of clones consistently produce elongated, organized structures.

While prior work has framed heterogeneity in embryonic stem (ES) cell populations as a liability that must be buffered or controlled[7], we use multicolor lineage tracing and spatial transcriptomics to propose that fate biases among individual clones can actively enhance patterning fidelity by guiding their spatial contributions. Clones appear to divide labor, making distinct contributions necessary for proper morphogenesis. Cellular diversity within the starting aggregate may mirror natural heterogeneity in the early embryo[64,65].

Our spatial transcriptomics experiments revealed that pure-clone gastruloids showed disrupted spatial organization of marker genes, with lower Moran's I values indicating poor spatial clustering, and positive L-metric values revealing coexpression of normally mutually exclusive anterior and posterior markers like *T* and *Igfbp5*. Such a "confused" gene expression pattern suggests that when clones are forced to generate all cell types rather than specializing in their preferred fates, they produce cells with mixed identity signatures.

Importantly, combining clones largely rescued defects in spatial gene expression. Chimeric gastruloids showed Moran's I values similar to bulk controls and restored mutual exclusivity between anterior and posterior markers. However, some residual signatures of propensity persisted even in successful chimeric gastruloids, with clone identity still detectable through subtle differences in marker gene expression levels. For instance, chimeric gastruloids composed of posterior clone 1 and posterior clone 6 exhibited relatively sparse expression of the anterior marker *Igfbp5*, consistent with both clones' posterior propensity. In gastruloids combining clone 1 with anterior clone 3, cells from clone 3 occasionally coexpressed *Igfbp5* and *T*. Thus, clones preferentially contribute to lineages aligned with their propensity, but retain molecular signatures of their intrinsic propensity even when filling misaligned roles.

Signatures of propensity become most apparent when clones must deviate from their preferred roles. Just as clone 3 cells revealed their anterior identity by maintaining *Igfbp5* expression in *T*-expressing populations, clones with a propensity for ectoderm formation *in vivo* showed stronger expression of ectodermal markers within ectoderm-derived tissues, whereas clones less likely to form ectoderm expressed mesoderm markers in these tissues. We therefore propose a model whereby clones' propensities guide their roles in development and form a basis for how they organize their respective fates.

Our findings align with recent work by Regalado et al.[34], which highlights how individual mES cells are remarkably heterogeneous, forming monoclonal gastruloids that can be biased toward mesodermal, neural, or other lineages. Relatedly, work from McNamara et al.[41] showed that differential Wnt signaling activity can shape individual cell contributions to gastruloids. These studies and others[47,62] point to the existence of heterogeneity in differentiation decisions among ES cells, but leave open the question of how heterogeneity is integrated across the population to produce consistent, reproducible morphogenetic outcomes. We connect lineage information with spatial gene expression, explicitly showing how lineage-dependent fate biases affect the spatial organization of tissues within the gastruloid.

What molecular differences among clones underlie their propensities? We found that clonal propensities were accompanied by subtle but reproducible differences in chromatin accessibility. In line with recent work[41,60,66],

differentially-accessible loci included those involved in Wnt and RA signaling. Interestingly, we observed that propensity degraded with passaging, suggesting that though persistent, it was not permanently encoded. In contrast, we observed that overall chromatin accessibility differences between clones with anterior propensity and those with posterior propensity persisted across passaging. It is possible that the majority (or even all) of these differences do not have functional consequences. Instead, it may be that only the specific epigenetic differences at developmentally relevant motifs drive propensity. We saw that chromatin accessibility differences at motifs related to Wnt, RA, and Nodal signaling were present even though clones retained similar expression of pluripotency-related genes, suggesting that the potential for propensity is present in chromatin landscapes even before overt lineage divergence.

Our ATAC-seq results indicate that clones' spatial propensities may reflect altered responsiveness to developmental cues like Wnt, RA, and Nodal signaling. Indeed, clones' propensities could be disrupted by RA and Nodal. RA treatment produced a "blended" phenotype where clone boundaries became indistinct and cells intermixed throughout the gastruloid, while Nodal inhibition maintained clear clonal boundaries but randomized their spatial arrangement along the A-P axis. These differential effects demonstrate that spatial propensity and sorting (segregation of clones from one another) can be uncoupled, and suggest that different signaling pathways regulate distinct aspects of clonal organization. Clones differ in how they interpret and respond to instructive signals, with consequences for tissue-level patterning under varying morphogen contexts.

Our findings notably point to cooperation among clones as a driving force for morphogenesis. Recent work[25,67] has pointed to bottlenecks in polyclonal aggregates that reduce clonal complexity. Moreover, *in vivo*, a wave of apoptosis in the epiblast precedes gastrulation[68]. It is not our view that these processes of cooperation and competition are mutually exclusive. In our study, chimeric aggregates did not show obvious evidence of clone takeover; perhaps, maximizing "collaborative" interactions among non-competitive clone combinations functions to eliminate potentially lethal lineage-specific defects, while allowing for proper morphogenesis via division of labor. Our findings build upon work by Braccioli et al.[69] who demonstrated that communication between tissues is essential for proper gastruloid development, showing that wild-type cells can rescue the developmental defects of transcription factor knockout cells through chimeric interactions. Our study shows that even among genetically identical stem cells, clonal diversity creates specialized subpopulations that spontaneously divide labor during gastruloid development. Cooperation among intrinsically biased clones may be a fundamental organizing principle that underlies communication among tissues.

The division of labor that we observed in gastruloids appears to operate on similar principles to the ability of pluripotent stem cells to rescue lethal organ deficiencies via blastocyst complementation. A number of emerging studies have explored the use of stem cells to promote the development of lungs[33], heart[70], liver[71], pancreas[31], and eyes[32], in embryos that were engineered to otherwise lack these organs. Exogenous stem cells could rescue organogenesis, preferentially forming cell types belonging to the organs that the embryos were unable to make themselves. Just like our observations in gastruloids, organogenesis *relied* on division of labor among a heterogeneous cell population in the context of rescuing organ development. Current regenerative medicine approaches often assume that homogeneous cell populations are optimal for therapeutic applications[72–74]. However, if natural development relies on coordinated heterogeneity, then therapeutic strategies might benefit from harnessing rather than eliminating cellular diversity. Our work establishing a framework for describing beneficial clonal interactions in development could inform the design of more effective stem cell therapies and tissue engineering approaches that use the ability of cells to cooperate.

Together, our findings position clonal heterogeneity as a substrate for self-organization. The key insight is that apparently similar pluripotent cells harbor subtle but functionally significant differences in their responsiveness to developmental cues. This principle may extend beyond gastruloids to other self-organizing systems. The combination of intrinsic cellular diversity with intercellular communication creates opportunities for emergent

properties that exceed the capabilities of individual components. Rather than requiring perfect uniformity, developmental precision may actually depend on the orchestrated behavior of diverse cellular players, each contributing their specialized capabilities to the collective task of morphogenesis.

Moving forward, systematically mapping how lineage priming intersects with tissue mechanics and morphogen dynamics could reveal general design principles underlying developmental precision that are shaped by the coordinated division of labor among cells.

Data and code availability

All raw and processed data, as well as code for analyses performed in this manuscript, can be found using this link:
https://www.dropbox.com/scl/fo/yklfs2p4s9dg8uyb6w8nt/ADXsVD7ABiklQnTyCSmhU5Q?rlkey=gl8drm3l79j9k7oi1wuro4s6w&st=87jmyzpt&dl=0

Acknowledgements

We thank all members of the Raj lab for scientific discussion and comments on the manuscript and data visualization. We thank Aoife O' Farrell and Miles Arnett for their discussion and assistance with the ATAC library preparation workflow, Yael Heyman and Grant Kinsler for their discussion and assistance with the seqFISH workflow, the William Greenleaf lab for sharing expertise in ATAC sequencing and providing us with custom primers used in our ATAC-seq experiments, and the Sydney Shaffer lab, particularly Sydney Shaffer, Christopher Coté, and Connor Hennessey, for assistance and equipment with sequencing and seqFISH. We thank the Jared Toettcher lab for their discussion and expertise with the gastruloid workflow, as well as for their gift of the E14-tg2a cell line. We thank Harry McNamara and Sedona Murphy for their helpful discussions and insights. Custom probes and kits for seqFISH experiments were designed by Spatial Genomics.

A.R. acknowledges support from a center grant from the Mark Foundation for Cancer Research, NIH Director's Transformative Research Award R01 GM137425, NIH R01 CA238237, NIH R01 CA232256, and NIH 4DN U01 DK127405. V.A. acknowledges support from NIH T32 148377. C.G.T. acknowledges support from the Damon Runyon Cancer Research Foundation, DRG-2465-22.

Author contributions

V.A. and A.R. conceived and designed the project under the supervision of A.R. V.A. designed and performed experiments with help from C.G.T. C.G.T designed and optimized lineage labels. K.S. generated Tn5 enzyme for ATAC-seq experiments. V.A. and A.R. wrote the manuscript with input from all authors. All authors read and approved the final manuscript.

Declaration of interests

A.R. receives royalties related to Stellaris RNA FISH probes. A.R. serves on the scientific advisory board of Spatial Genomics. A.R. is the founder of CytoPixel Software. All other authors declare no competing interests.

Declaration of generative AI and AI-assisted technologies

During the preparation of this work, the authors used ChatGPT and Claude to generate and improve code for analyses and to suggest improvements to the clarity and flow of the text. The authors reviewed and edited the content and take full responsibility for the content of the manuscript.

Figure Legends

Figure 1. mES cell clone diversity promotes gastruloid self-organization.
(A). Schematic describing gastruloid formation and our fluorescent lineage tracing scheme. mES cells expressing unique combinations of the fluorophores eGFP, mKate2, and mOrange2 are dilution cloned and expanded into clonal mES cell lines, which are then used to generate gastruloids.
(B) Gastruloid morphologies are classified as “elongated,” “multiaxial,” or “no axis”. Bargraphs represent the proportion of gastruloids within each batch of aggregation classified as belonging to a given class of morphologies (n=8-33 gastruloids per batch). The scale bar represents 100px. Annotations (A) and (P) label the gastruloid anterior and posterior, respectively. Each experiment was assigned an “aggregation batch number.” Experiments presented in this panel included pure clone gastruloids and bulk gastruloids; gastruloids aggregated on the same day share a batch number to enable comparison of pure clone morphologies to bulk gastruloids from the same day/plate.
(C) Representative Incucyte images of clone-bulk combinations are shown, alongside line graphs showing the normalized (as described in **Methods**) fluorescence intensity along the gastruloid A-P axis. Bold lines show the average intensity profile for gastruloids within a given batch, and error ribbons represent one standard deviation. The scale bar represents 100px.
(D) 300-cell chimeric aggregates where 100%, 50%, or 25% of the cells belong to a given clone and the remainder of the cells belong to the bulk were generated. Bargraphs showing the average fraction of gastruloids that are “elongated” for each chimeric combination are shown. A dotted red line depicts the average fraction of gastruloids that are “elongated” across aggregation batches.
(E) Three representative images for each combination of clones. Shown are pairings of anterior-biased clones with posterior-biased clones, anterior-biased clones with anterior-biased clones, and posterior-biased clones with posterior-biased clones. The scale bar represents 100px.

Figure 2. Spatial transcriptomics reveals patterns of gene expression underlying morphologies of pure-clone gastruloids.
(A) Schematic describing the experimental workflow. seqFISH was performed on gastruloids made from bulk mES cells and from labeled mES cell clones.
(B) Representative images showing the expression of *T* (blue) and *Igfbp5* (gold) in gastruloids made from bulk mES cells or mES cell clones 1, 3, and 6. Insets highlight examples where cells are coexpressing *T* and *Igfbp5*, or highlight posterior *Igfbp5* expression or anterior *T* expression.
(C) Quantification of Moran’s I across bulk and pure-clone gastruloids (bulk: n=2, posterior clone 1: n=5, anterior clone 3: n=5, posterior clone 6: n=2) within a batch. Representative gastruloids, where cells are colored on the basis of their *Cyp26a1*, are shown above.
(D) Quantification of the L-metric across bulk and pure-clone gastruloids within the same batch. Representative hexbin plots are shown, comparing the expression of *T* and *Igfbp5* in selected gastruloids.
(E) Quantification of Moran’s I across bulk and chimeric gastruloids from a second seqFISH batch (bulk: n = 2, clone 1+3: n = 2, clone 1+6: n = 3).
(F) Quantification of L-metric across bulk and chimeric gastruloids from this second seqFISH batch. A representative hexbin plot of *T* and *Igfbp5* expression from a selected clone 1+3 gastruloid is shown, alongside an image of a cell from this gastruloid coexpressing *T* and *Igfbp5*.

Figure 3. Propensity decreases across passages.
(A) Representative images and quantification of changes in clones’ propensity across three rounds of passaging. Gastruloids from the combination of clone 1 and clone 3 are shown. Scale bars represent 100px.
(B) Schematic describing isolation of subclones from mES cell clones.
(C) Individual fluorescence intensity curves for every gastruloid generated from each subclone isolated from clone 1 and clone 3 at passage 1 and at passage 2. Normalization is described in **Methods**.

Figure 4. ATAC-seq and RNA-seq of mES cell clones show differences in chromatin accessibility associated with propensity.
(A) Schematic describing the workflow for harvesting samples for RNA-seq and ATAC-seq.
(B) Volcano plot showing differentially-expressed genes between anterior clones and posterior clones.

(C) Bargraph comparing the expression of pluripotency markers among bulk mES cells, anterior clones, and posterior clones.
(D) Bargraph comparing the expression of marker genes for cell types expected to be present in gastruloids.
(E) Volcano plot showing genes near differentially-accessible genomic regions between anterior clones and posterior clones.
(F) Representative ATAC-seq tracks for Fbxw26 and Sp5, genes with genomic regions more accessible in anterior clones.
(G) Upset plots showing the number of peaks unique to posterior clones, anterior clones, or bulk mESCs or peaks shared among these samples. Plots are shown for samples harvested at passage 1 and at passage 3.
(H) Scatterplots showing motifs identified by HOMER as being more enriched among peaks more accessible in anterior clones than posterior clones at passage 1. The x-axis shows enrichment scores: the fold-change between the proportion of sequences containing each motif among differentially accessible peaks versus the proportion of sequences containing each motif among peaks randomly selected through the mouse genome. The y-axis shows adjusted p-values. Labeled peaks have enrichment scores > 2.5 and adjusted p-values < 0.05.
(I) Barplots comparing motif enrichment scores across passages, for each motif annotated as significant in **(H)**.

Figure 5. Perturbing Nodal signaling disrupts clones' propensity while maintaining their sorting.
(A) Schematic describing how cells might sort if they have propensity, how cells might lack propensity and fail to sort, or might sort without having propensity.
(B) Representative images of gastruloids comprising clone 1 and clone 3 under control conditions, or when treated with retinoic acid or SB431542 (Nodal inhibitor) from 96-120 hours after aggregation.
(C) Line scans describing the fluorescence intensities in red and green channels along the A-P axis for gastruloids under each condition. Normalization is described in **Methods**. Here, the mean of each line scan was subtracted to enable direct comparison of variation within each condition. Fluorescence intensities in the red channel were scaled to match the range of green fluorescence intensities. Scale bars for corresponding images correspond to 50px.
(D) Quantification of the effect of chemical perturbation on gastruloid sorting. The fraction of the gastruloid anterior occupied by a given clone, minus the fraction of the gastruloid posterior occupied by that clone, is plotted for clone 1 and clone 3. Asterisks denote statistical significance comparing differences to zero (* $p<0.05$, ****$p<0.0005$).
(E) Workflow for computing IOU. Masks for each channel are shown, along with composite images displaying masks for both channels (YFP colored in green, Cy3 colored in red). The region of overlap between masks is also shown, along with the IOU for each representative example.
(F) Boxplots displaying IOU values for gastruloids under each condition. Asterisks denote statistically significant differences between conditions (* $p<0.05$, ****$p<0.0005$).
(G) Stacked barplots showing the percentage of gastruloids that are elongated, multiaxial, or that have no axis. The plot shows bulk mES cells under control conditions, treated with RA, or treated with Nodal inhibitor and clone 1+3 gastruloids under control conditions, treated with RA, or treated with Nodal inhibitor.

Figure 6. Analysis of an *in vivo* lineage tracing dataset reveals persistent bias through development.
(A) Schematic depicting the conceptual workflow.
(B) The fraction of cells belonging to ectoderm-derived tissues for three clones in the dataset.
(C) For only cells annotated as belonging to ectoderm, derived tissues, barplots are shown comparing gene expression values for ectoderm markers (*top*) and mesoderm markers *(bottom*), comparing the top 4 clones with the highest proportion of cells in ectoderm tissues and the 4 clones with the lowest proportion of cells in ectoderm tissues.
(D) For only cells annotated as belonging to posterior mesoderm, derived tissues, barplots are shown comparing gene expression values for mesoderm markers (*top*) and ectoderm markers *(bottom*), comparing the top 4 clones with the highest proportion of cells in posterior mesoderm tissues and the 4 clones with the lowest proportion of cells in posterior mesoderm tissues.

Materials and Methods

Cell Culture

Experiments were performed using cell lines generated from E14-tg2a mouse embryonic stem cells (ATCC CRL-1821). mES cells were thawed and plated on 25cm^2 cell culture flasks coated with 0.1% gelatin. Cells were grown in 2i + LIF media comprising GMEM (Millipore Sigma, G6148) supplemented with 10% ESC qualified fetal bovine serum (R&D Systems, S10250), 1x GlutaMAX (Gibco, 35050–061), 1x MEM non-essential amino acids (Gibco, 11140– 470 050), 1 mM sodium pyruvate (Gibco, 11360–070), 100 μM 2-mercaptoethanol (Gibco, 471 21985–023), and 100 units/mL penicillin/streptomycin (Gibco, 15140–122), 1000 units/mL LIF (Millipore 473 Sigma, ESG1107), 2 μM PD0325901 (Tocris, 4192), and 3 μM CHIR99021 (Tocris, 4423). Cells were maintained between 20% and 80% confluency and were passaged by aspirating growth media, washing with phosphate buffered saline (PBS, Gibco, 14190144), and trypsinizing for 5 minutes at 37C (TrypLE Express, Gibco, 12605028). Trypsin was quenched with 2i+LIF media and cells were subsequently centrifuged at 500rpm for 5 minutes and pelleted. Supernatant was aspirated and cells were resuspended in fresh media prior to replating. Passage ratios varied from 1:5 to 1:10.

For experiments involving bottlenecked mES cell clones, cells from a polyclonal population were passaged into 96-well plates at a density of 1 cell per well. These were grown for ~2 weeks and colonies were imaged using an Incucyte S3 Live Cell Imaging Analysis System (Sartorius) with a 4× objective. Viable colonies were serially expanded into 24-well, 6-well plates and then 25cm^2 cell culture flasks. These were allowed to grow before being used for experiments or frozen down for subsequent analysis. With the exception of experiments testing late-passage clones, experiments were performed on clones passaged 1-2 times after freezing, and vials were frozen at each round of passaging. Cell cultures were mycoplasma negative.

Gastruloid Protocol

Gastruloids were grown in N2B27 media (1:1 mixture of DMEM/F-12 (Gibco, 11320033) and neurobasal medium (Gibco, 21103049), supplemented with 100 μM 2-mercaptoethanol, 1:100 N-2 (Gibco, 17502048), 1:50 B-27 (Gibco, 17504044), and 100 units/mL penicillin/streptomycin (Gibco, 15140–122)). E14-tg2a cells were trypsinized and pelleted, then washed twice with PBS with each wash followed by a 5-minute centrifugation at 500rpm. Cells were resuspended in N2B27 media and counted. To form gastruloids, 300 single cells in 40μl N2B27 media were pipetted into each well of an ultra-low attachment 96-well round-bottom microplate (Corning, 7007). These plates were then transferred to a cell culture incubator for 48h, after which each aggregate was administered 140μL of N2B27 media supplemented with 3μM Chiron. Media was replaced with 140μl fresh N2B27 without Chiron 24 hours afterward (at 72 hours after aggregation), and subsequently every 24 hours for the remaining 48 hours of the gastruloid protocol. Gastruloids were assayed either by imaging using an Incucyte, or by immunofluorescence, in which case samples were fixed for 2 hours in 4% PFA at 4 °C before being washed twice with PBS, or by seqFISH in which samples were fixed in 4% PFA before being permeabilized in 70% ethanol before embedding.

Lineage Labeling

To generate the nuclear-localized fluorescent reporter constructs, eGFP, mOrange2, and mKate2 fluorescent proteins were cloned into a lentiviral backbone under the control of the EF1α promoter, as has been described[75]. Sequences encoding fluorophores were flanked by the SV40 nuclear localization signal. The constructs included the woodchuck hepatitis virus posttranscriptional regulatory element (WPRE). A β-lactamase (AmpR) resistance gene was used for bacterial selection.

Plasmids were amplified using plasmid electroporation into Endura electrocompetent Escherichia coli cells (Lucigen) using a Gene Pulser Xcell (Bio-Rad). An AmpR resistant clone was isolated and grown at 32 °C for 12-14 hours with agitation. Plasmids were isolated from the pelleted cells using the EndoFree Plasmid Maxi Kit (Qiagen, 12362) per the manufacturer's protocol.

Lentivirus was produced by transfecting Lenti-X 293T cells with helper plasmids VSVG and psPAX2 using polyethylenimine (Polysciences 23966) in Opti-MEM (Thermo Fisher, #31985062). A mass ratio of 4:2:3 for plasmid DNA:VSVG:psPAX2 was used. The transfection mix was mixed and incubated for 15 minutes at room temperature before being added dropwise to the cell monolayer. Lentivirus was collected 24, 48, and 72 hours after transfection, pooled, filtered, and concentrated using ultracentrifugation. Lentiviral stocks were stored at −80 °C.

Morphology Analysis

Experiments were conducted on an Incucyte S3 Live Cell Imaging Analysis System (Sartorius) with a 4× objective. Phase and fluorescence images were acquired, with 300ms exposure for GFP and 400ms exposure for mCherry. Images were exported as 8-bit TIFs for phase images and 16-bit TIFs for fluorescent images. A custom script (https://github.com/arjunrajlaboratory/process_incucyte_tiff_data) was used to upload and analyze data with NimbusImage (https://www.nimbusimage.com/).

Gastruloid segmentation was performed manually, and gastruloids were annotated as "normal" if they were elongated along a single axis, "multiaxial" if multiple axes of elongation or projections were present, and "no symmetry breaking" if no obvious axis had formed or if gastruloids assumed irregular shapes.

For experiments involving chimeric gastruloids, a line was drawn along the gastruloid's long axis, and fluorescent intensities were measured along the length of each line. NimbusImage annotations were exported in JSON format, and fluorescence line-scans were exported as CSVs for subsequent analysis. The posterior region of the A-P axis was defined either by expression of T (eg, in immunofluorescence experiments, below) or manually by gastruloid morphology. Samples that were not amenable to this line-scan analysis or A/P annotation due to a failure to elongate or due to a lack of any clear anteroposterior axis were excluded from analysis. For plots including individual line scans and multiple channels (eg, red and green), the green channel was scaled down since intensity measurements in this channel were consistently higher. This scaling factor was 10 by default, and 20 for batches 1 and 3 in line scans showing the effect of RA treatment and Nodal inhibition.

Clones 2 and 4 were excluded from analyses of propensity due to their dim fluorescence. Gastruloids generated from clone 2 (red) occasionally lost fluorescence as it elongated, making assessment of propensity unreliable. While clone 4 (red) did often appear in the posterior of chimeric gastruloids generated from bulk and clone 4 (**Supplementary Figure 2F**), it was also very dim, and hence hard to tell apart from background in many/most images of chimeric gastruloids.

Gastruloid Embedding

Gastruloids were fixed as described above in 4% PFA (2 hours for experiments involving pure clone gastruloids, as these were done alongside immunofluorescence, and 15 minutes for experiments involving combined-clone gastruloids) before being transferred to 70% ethanol. Gastruloids were first pooled in a low-bind tube and then washed with buffer containing 10% formamide, 2x SSC, and 0.2% tween-20, and then with PBS with 0.2% tween-20 10mL of a gel solution including 750µl of 5M NaCl, 625µl of 1M Tris-HCL, 1250µl of 40% bis-acrylamide and 9.9ml water was made. Gastruloids were resuspended in 30µl of gel, activated using 37.5 µl of 10% ammonium persulfate and 18.75µl tetramethylethylenediamine (TEMED), and spotted onto proprietary functionalized coverslips made by SpatialGenomics, anchored by a coverglass coated with

GelSlick (Lonza, #50640). Embedded gastruloids were incubated at 37 °C for 2 hours. Samples were washed with PBS, covered with 8% SDS and allowed to incubate for 1 minute before being washed again with PBS and incubated for 1 hour at 37 °C with Proteinase K (Thermo Fisher, #EO0491, 3µl diluted into 3mL of PBS with 2% Tween-20, diluted 100-fold further into 8mL PBS with Tween-20). Samples were washed with PBS twice, and primary probes were added to each sample, which was incubated at 37 °C for 24 hours. Slides were next used to assemble a flow cell (components provided by SpatialGenomics), rinsed with a wash buffer, incubated with DAPI for 1 hour at 37 °C, and washed with a kit-provided rinse buffer before imaging.

Sequential FISH

Spatial transcriptomics experiments were performed using sequential FISH using technology from SpatialGenomics. We used a small custom panel of marker genes guided by recent single-cell RNA-seq studies[47]: *T*, *Hoxc8*, *Hoxb9*, *Sox2*, *Cyp26a1*, *Igfbp5*, *Wnt3*, *Sfrp1*, *Ncam1*, *Sox9*, *Lhx1*, *Nrp2*, *Thy1*, *Gbx2*, *Pim2*, *Utf1*, *Zfp42*, *Mesp1*, *Epha5*, *Hoxaas3*. The panel was designed in collaboration with SpatialGenomics and synthesized by them. All genes were identified sequentially via single-molecule FISH. seqFish was performed using SpatialGenomics' GenePS instrument (software v1.6.0), and images were acquired at a z-offset of 1-2µm to ensure adequately-focused nuclei and spot detection.

Sequential FISH analysis

All image processing was done either on the GenePS machine or with SpatialGenomics' proprietary software (software v0.9.0). Raw images were aligned across multiple rounds of hybridization to form composite images, and each channel was manually thresholded before spot-counting. In each experiment, genes that were either poorly detected or had high background were removed from the analysis. Transcript identities were decoded, and nuclei were segmented using DAPI images (or GFP images, for experiments involving segmenting only clone 1) via CellPose[76,77]. A mask was formed from segmented nuclei that included the nucleus plus a dilation around the nucleus, allowing individual transcripts to be assigned to individual cells, yielding a cell-by-gene count matrix along with nuclear xy-locations. For chimeric gastruloids where clone 1 was segmented, each cell was segmented using DAPI and GFP, as above, so for each GFP-annotated cell, the closest DAPI-annotated cell was annotated as belonging to clone 1. Subsequent analysis included the custom SGAnalysis package (https://github.com/arjunrajlaboratory/SGanalysis). Moran's I was calculated using the *lctools* package in R.

L-metric scores were computed using the custom l-metric package (https://github.com/arjunrajlaboratory/l-metric). For each cell, counts from each pair of genes are read in, yielding a list of gene expression values for both genes across all cells in the dataset. These were sorted on the basis of the first gene in the pair. Three vectors were generated for gene 2: one exclusively containing the mean expression of gene 2, another sorted from lowest to highest, and a third sorted from highest to lowest. Cumulative sums for gene 1 and gene 2 (sorted on the expression of gene 1) are computed to compare how gene 2 accumulates relative to itself, a flat line, and the low-to-high and high-to-low-ranked vectors. The area between the cumulative sum for gene 2 and the flat line is computed and normalized by the low-to-high and high-to-low-ranked vectors. Negative values correspond to mutually exclusive gene expression, resulting in an L-shaped scatter of gene 1 vs. gene 2, and positive values correspond to coexpression of gene 1 and gene 2.

To further compare coexpression patterns between experimental groups, we used permutation testing based on pairwise Jensen-Shannon divergence (JSD). For each pair of genes, we computed a two-dimensional histogram over a fixed 100-by-100 bin grid spanning the central 98% of the pooled expression range among all samples. Histogram counts were normalized to sum to 1 to produce a discrete probability distribution over the joint gene expression space for each gastruloid. We then computed the Jensen-Shannon divergence between each pair of histograms, labeling these as within-group (e.g., bulk sample vs. bulk sample) or between-group (e.g., bulk vs. clone 3). We used the difference between the mean within-group and between-group JSDs as a

test statistic. We then performed a nonparametric permutation test whereby group labels were shuffled 5000 times, computing the test statistic at each permutation to generate a null distribution. The p-value was computed as the proportion of permuted test statistics greater than or equal to the observed test statistic.

Immunofluorescence of mES Cell Monolayers

Cells, plated on 24-well imaging plates (P24-0-N), were fixed in 70% ethanol and stored at 4C. For immunofluorescence, ethanol was aspirated and samples were washed with PBS and incubated for 5 minutes at room temperature. Samples were then washed with PBS with 0.1% Triton-X reagent. Samples were then incubated for 1 hour with primary antibody (anti-beta catenin: mouse anti-beta catenin antibody, Invitrogen #13-8400, anti-Sox17: goat anti-Sox17 antibody, R&D #AF1924; anti-T/Brachyury: Human/Mouse Goat anti-Brachyury, R&D #AF2085; anti-Pax6: rabbit anti-Pax6 antibody, Abcam ab195045) for 1 hour at a 1:200 dilution in PBS. Samples were then washed 3x with PBS with 0.1% Triton-X reagents, with 5 minutes in between washes. We then incubated for another hour with secondary antibody (A488 anti-mouse, Cell Signaling Technologies #4408S; A594 anti-mouse, Cell Signaling Technologies #8890; A488 donkey anti-sheep, Life Technologies #A11015; A647 goat anti-rabbit, Invitrogen #A21244) at a 1:400 dilution in PBS. Samples were then washed 3x with PBS, with 5 minutes in between washes. For the second PBS wash, DAPI was added. PBS was replaced with 2xSSC, and samples were imaged at 20X on a Nikon Ti-E with a 10X Plan-Apo objective with filter sets for Cy3, Atto647N, Alexa594, and Alexa488. Images were acquired with a 0.45 numerical aperture.

Gastruloid Immunofluorescence

Gastruloids were fixed in 4% PFA for 2 hours at 4C as described above and transferred to PBS with 0.2% Triton-X (PBST) for overnight incubation at 4C. We next added primary antibody (Human/Mouse Goat anti-Brachyury, R&D #AF2085) at a 1:400 dilution and incubated overnight at 4C. We next washed out the primary antibody, first with three back-to-back washes with PBSFT, followed by three washes of PBSFT spaced 1 hour apart, to allow the primary antibody to diffuse out of the gastruloid. We next administered secondary antibody (A647 donkey anti-sheep, Invitrogen #A21448) at a 1:400 dilution and incubated overnight at 4C. Next, we again washed out the secondary antibody with three back-to-back PBSFT washes, followed by three washes of PBSFT spaced 1 hour apart before imaging. Samples were then transferred to a glass-bottom 8-chambered imaging slide for imaging (Cellvis C8-1-N). Samples were imaged on a Nikon Ti-E with a 10X Plan-Apo objective with filter sets for Cy3, Atto647N, Alexa594, and Alexa488. Images were acquired with a 0.45 numerical aperture objective.

Gastruloid Live Imaging

Gastruloids were immobilized in Matrigel for live imaging. Matrigel matrix (Corning #356231) was thawed overnight at 4 °C. Glass bottom 8-chambered imaging slides were chilled to 4C, and each chamber was coated with Matrigel reagent and then transferred to ice. Gastruloids were collected using 200µl pipette tips with the ends cut off and dispersed into the cooled Matrigel within each chamber. Slides were then warmed at 37 °C for 10 minutes to solidify the Matrigel, and 100µl N2B27 medium was added to each chamber. Samples were imaged using a Nikon Ti-E with a 4X or 10X Plan-Apo objective and kept in a microscope-mounted environmental chamber with controlled temperature, CO_2, and humidity. Images were acquired every 60-90 minutes over 24-48 hours. Images were maximum-intensity projected to generate final movies.

Differentiation Assay

For endoderm induction[78], DMEM (Thermo Fisher, 11995065) was supplemented with 0.5% ESC-qualified fetal bovine serum, 100ng/mL activin A (Fisher Scientific 338AC010), and GlutaMAX. For mesoderm induction, DMEM was supplemented with 20ng/mL BMP4 (Fisher Scientific 315-27), 0.5ng/mL activin A, and 2.5ng/mL

bFGF (Fisher Scientific PHG0367). For neural induction, we cultured cells in Neurobasal medium with Neural Induction Supplement (Gibco A1547701). Cells were trypsinized and plated at a density of 50,000 cells/well in 24-well glass-bottom plates (CellVis P24-0-N) containing the respective induction media. Cells were imaged every 24 hours for 72 hours following plating, and the media was refreshed every 24 hours.

RNA sequencing and analysis

We sequenced mRNA from clonal E14-tg2a mES cell lines. As clones were expanded, cells were collected at a density of 75,000 cells per sample and stored in QIAzol. Samples from a bulk population were also harvested as a control. RNA was extracted (Direct-zol RNA-mini kit, Zymo Research, #R2072) We used the Watchmaker mRNA library prep kit, indexing samples using xGen Stubby Adapter-UDI primers for Element (IDT, #10017037) and sequenced each sample at a depth of ~20 million reads on an Element AVITI sequencing instrument (75+75bp, high-output Cloudbreak Freestyle). We pseudoaligned reads to mm10 using *Kallisto* and imported the output into R via *tximport*. We used the Relative Log Expression (RLE) and calculated counts per million (CPM) per gene. To compare the expression of pluripotency markers between clonal mES cells and bulk, the genes *Dnmt3l*, *Dppa3*, *Dusp6*, *Esrrb*, *Klf4*, *Myc*, *Nanog*, *Otx1*, *Pou5f1*, *Sox2*, *Tet2*, *Utf1*, *Zfp42*, and *Zic2* were used. To compare expression of gastruloid cell type markers, we used the genes *Igfbp5*, *Gata6*, *Aldh1a2*, *Hoxd4*, *Hoxb9*, *Hoxc8*, *Wnt3a*, *Cyp26a1*, *Sox2*, and *T*.

ATAC sequencing

We performed ATAC sequencing based on a modified protocol based on the Omni-ATAC-seq method[79]. At each round of passaging that we tested, we collected 50,000 cells per technical replicate and lysed these in a buffer containing 10% NP-40, 10% Tween-20, and 1% Digitonin for 3 minutes at 4C. We transposed lysed cells with Tn5 (a gift from Dr. Kavitha Sarma, Wistar Institute) for 30 minutes at 37 °C. Transposed DNA was isolated using a Zymo DNA Clean and Concentrator kit, and then amplified using custom primers (**Supplemental Table 1**, originally designed by Greenleaf Lab, Stanford University) for 13 PCR cycles. Libraries were purified using double-sided selection with AMPure XP magnetic beads, and quantified using BioAnalyzer High Sensitivity DNA chips. We sequenced libraries at a depth of ~50 million paired-end reads per sample on a NextSeq2000 with a P4 XLEAP 100-cycle kit.

ATAC sequencing analysis

After aligning reads to mm10 using bowtie2. We called peaks using MACS3 (version 3.0.3), keeping an FDR cutoff of 0.001 and filtering to a fragment size less than 150bp. We generated one nonredundant peak list filtered to those found in at least two samples and that were not listed in the ENCODE blacklist. We then used GenomicAlignment's *summarizeOverlaps* function to generate a counts matrix that included all samples. Peaks were annotated using *annotatePeak* from the ChIPseeker package[80] and were mapped to their closest gene transcription start site. Upset plots were generated after making peak lists where, for each condition, at least one technical replicate had that peak for all clones within that condition. We performed differential peak analysis using DEseq2. For all comparisons tested, we extracted a peak list of differential peaks ($|\log2FC| > 1$) and used this peak list as input to HOMER[81], using default parameters for de novo motif discovery.

Channel IOU Analysis

To test whether different chemical perturbations affected patterning of clones beyond their arrangement along the A-P axis, we segmented gastruloids and generated masks within each channel using Otsu thresholding, via the scikit-image Python package[82]. The number of pixels shared within fluorescent channel masks was computed as the intersection between those masks, and the number of pixels included within the composite of the masks defined the union of those masks. The quotient between intersection and union was compared across experimental conditions.

Re-analysis of Weber et al.

We analyzed a publicly available single-cell RNA-seq dataset generated by Weber et al[63]. The dataset came annotated, such that each cell had been assigned its clone barcode and a tissue type. We assigned each tissue type to its germ layer of origin. Ectoderm was assigned to migrating neural crest, enteric neurons, differentiating neurons, dorsal root ganglia, neuronal/glial progenitors, GABAergic neurons, neural crest, and neuroblasts. Endoderm was assigned to epithelial cells. Anterior mesoderm was assigned to pulmonary/gastrointestinal mesenchyme, ovarian mesenchyme, smooth muscle, valve/endocardial cushion, perivascular cells, myocardium, mesentery/epicardium, fibroblast pole, and erythrocytes - definitive. Posterior mesoderm was assigned to renal mesenchyme, nephron progenitor, musculoskeletal mesenchyme, skeletal muscle, erythrocytes - primitive, tendon/ligament pole, chondrocyte pole, pericytes, meningeal fibroblasts, and skeletal mesenchyme. Mesoderm, mixed, was assigned undifferentiated/proliferative mesenchyme, megakaryocytes/hematopoietic progenitors, and macrophages. We filtered clones on the basis of a dataset-provided exclusion list, and to remove barcodes with fewer than 5 cells assigned. The proportion of cells within each germ layer was calculated for each clone. Clones were then ranked on the basis of the fraction of their cells that belong to ectoderm-derived tissues.

We next subset our cell-by-gene matrix to only include cells from, respectively, ectoderm, or in another analysis, posterior mesoderm. Expression of ectoderm/anterior genes *Hes5, Btg2, Cenpf, Chrd, Nog, Nes, Zic2, Hoxa1, Pax6, Sfrp1, Dkk1, Tbx1*; and posterior mesoderm genes *Foxf1, Foxc1, Foxd1, Pbx1, Meis2, Mest, Cdh2, Hoxc10, Hoxd11*, *Eomes* was compared across clones.

References

1. Merle, M., Friedman, L., Chureau, C., Shoushtarizadeh, A., and Gregor, T. (2024). Precise and scalable self-organization in mammalian pseudo-embryos. Nat. Struct. Mol. Biol. https://doi.org/10.1038/s41594-024-01251-4.

2. Raj, A., and van Oudenaarden, A. (2008). Nature, nurture, or chance: stochastic gene expression and its consequences. Cell *135*, 216–226.

3. Zernicka-Goetz, M., Morris, S.A., and Bruce, A.W. (2009). Making a firm decision: multifaceted regulation of cell fate in the early mouse embryo. Nat Rev Genet *10*, 467–477.

4. Waddington, C.H. (1942). CANALIZATION OF DEVELOPMENT AND THE INHERITANCE OF ACQUIRED CHARACTERS. Nature *150*, 563–565.

5. Rutherford, S.L., and Lindquist, S. (1998). Hsp90 as a capacitor for morphological evolution. Nature *396*, 336–342.

6. Raj, A., Rifkin, S.A., Andersen, E., and van Oudenaarden, A. (2010). Variability in gene expression underlies incomplete penetrance. Nature *463*, 913–918.

7. Torres-Padilla, M.-E., and Chambers, I. (2014). Transcription factor heterogeneity in pluripotent stem cells: a stochastic advantage. Development *141*, 2173–2181.

8. Huang, S. (2009). Non-genetic heterogeneity of cells in development: more than just noise. Development *136*, 3853–3862.

9. Martinez Arias, A., and Brickman, J.M. (2011). Gene expression heterogeneities in embryonic stem cell populations: origin and function. Curr Opin Cell Biol *23*, 650–656.

10. Johnston, R.J., Jr, and Desplan, C. (2010). Stochastic mechanisms of cell fate specification that yield random or robust outcomes. Annu Rev Cell Dev Biol *26*, 689–719.

11. Genuth, M.A., Kojima, Y., Jülich, D., Kiryu, H., and Holley, S.A. (2023). Automated time-lapse data segmentation reveals in vivo cell state dynamics. Sci Adv *9*, eadf1814.

12. Ainsworth, J., Zhao, Y., Gao, K., Gravina, N.M., Goldberg, Z.H., Pinkerton, C., Rifkin, S.A., Ernst, A.M., Garcia, H.G., and Perry, M.W. (2025). Cell fate ratios are encoded by transcriptional dynamics in the Drosophila retina. Curr Biol. https://doi.org/10.1016/j.cub.2025.05.037.

13. Arias, A.M., Marikawa, Y., and Moris, N. (2022). Gastruloids: Pluripotent stem cell models of mammalian gastrulation and embryo engineering. Dev. Biol. *488*, 35–46.

14. Anlaş, K., Gritti, N., Nakaki, F., Salamó Palau, L., Tlili, S.L., Oriola, D., Arató, K., Lim, J.L., Sharpe, J., and Trivedi, V. (2024). Early autonomous patterning of the anteroposterior axis in gastruloids. Development *151*. https://doi.org/10.1242/dev.202171.

15. Martyn, I., Kanno, T.Y., Ruzo, A., Siggia, E.D., and Brivanlou, A.H. (2018). Self-organization of a human organizer by combined Wnt and Nodal signalling. Nature *558*, 132–135.

16. Turner, D.A., Girgin, M., Alonso-Crisostomo, L., Trivedi, V., Baillie-Johnson, P., Glodowski, C.R., Hayward, P.C., Collignon, J., Gustavsen, C., Serup, P., et al. (2017). Anteroposterior polarity and elongation in the absence of extra-embryonic tissues and of spatially localised signalling in gastruloids: mammalian embryonic organoids. Development *144*, 3894–3906.

17. Sendra, M., McDole, K., Jimenez-Carretero, D., de Dios Hourcade, J., Temiño, S., Raiola, M., Guignard, L., Keller, P.J., Sánchez-Cabo, F., Domínguez, J.N., et al. (2024). Epigenetic priming of embryonic lineages in the mammalian epiblast. bioRxiv, 2024.01.11.575188. https://doi.org/10.1101/2024.01.11.575188.

18. Marks, H., Kalkan, T., Menafra, R., Denissov, S., Jones, K., Hofemeister, H., Nichols, J., Kranz, A., Stewart, A.F., Smith, A., et al. (2012). The transcriptional and epigenomic foundations of ground state pluripotency. Cell *149*, 590–604.

19. Klein, A.M., Mazutis, L., Akartuna, I., Tallapragada, N., Veres, A., Li, V., Peshkin, L., Weitz, D.A., and Kirschner, M.W. (2015). Droplet barcoding for single-cell transcriptomics applied to embryonic stem cells. Cell *161*, 1187–1201.

20. Kalmar, T., Lim, C., Hayward, P., Muñoz-Descalzo, S., Nichols, J., Garcia-Ojalvo, J., and Martinez Arias, A. (2009). Regulated fluctuations in nanog expression mediate cell fate decisions in embryonic stem cells. PLoS Biol *7*, e1000149.

21. Lineages of embryonic stem cells show non-Markovian state transitions (2021). iScience *24*, 102879.

22. Wolpert, L. (1989). Positional information revisited. Development *107*, 3–12.

23. Díaz-Díaz, C., Fernandez de Manuel, L., Jimenez-Carretero, D., Montoya, M.C., Clavería, C., and Torres, M. (2017). Pluripotency Surveillance by Myc-Driven Competitive Elimination of Differentiating Cells. Dev Cell *42*, 585–599.e4.

24. Lima, A., Lubatti, G., Burgstaller, J., Hu, D., Green, A.P., Di Gregorio, A., Zawadzki, T., Pernaute, B., Mahammadov, E., Perez-Montero, S., et al. (2021). Cell competition acts as a purifying selection to eliminate cells with mitochondrial defects during early mouse development. Nature Metabolism *3*, 1091–1108.

25. Frenster, J.D., Babin, S., Josende Garcia, J.B., Casani Galdon, P., Pascual-Mas, P., Robertson, G., Garcia Ojalvo, J., and Martinez Arias, A. (2025). A mosaic gastruloid model highlights the developmental stage-specific restriction of cell competition in mammalian

pre-gastrulation. bioRxiv, 2025.01.25.634859. https://doi.org/10.1101/2025.01.25.634859.

26. Arias, A.M., and Hayward, P. (2006). Filtering transcriptional noise during development: concepts and mechanisms. Nat Rev Genet *7*, 34–44.

27. Hölldobler, B., and Wilson, E.O. (1990). The Ants (Harvard University Press).

28. West, S.A., and Cooper, G.A. (2016). Division of labour in microorganisms: an evolutionary perspective. Nat Rev Microbiol *14*, 716–723.

29. Janiszewska, M., Tabassum, D.P., Castaño, Z., Cristea, S., Yamamoto, K.N., Kingston, N.L., Murphy, K.C., Shu, S., Harper, N.W., Del Alcazar, C.G., et al. (2019). Subclonal cooperation drives metastasis by modulating local and systemic immune microenvironments. Nat Cell Biol *21*, 879–888.

30. Founta, K.-M., and Papanayotou, C. (2021). In Vivo Generation of Organs by Blastocyst Complementation: Advances and Challenges. International Journal of Stem Cells *15*, 113.

31. Matsunari, H., Nagashima, H., Watanabe, M., Umeyama, K., Nakano, K., Nagaya, M., Kobayashi, T., Yamaguchi, T., Sumazaki, R., Herzenberg, L.A., et al. (2013). Blastocyst complementation generates exogenic pancreas in vivo in apancreatic cloned pigs. Proceedings of the National Academy of Sciences *110*, 4557–4562.

32. Zhang, H., Huang, J., Li, Z., Qin, G., Zhang, N., Hai, T., Hong, Q., Zheng, Q., Zhang, Y., Song, R., et al. (2018). Rescuing ocular development in an anophthalmic pig by blastocyst complementation. EMBO Molecular Medicine. https://doi.org/10.15252/emmm.201808861.

33. Mori, M., Furuhashi, K., Danielsson, J.A., Hirata, Y., Kakiuchi, M., Lin, C.-S., Ohta, M., Riccio, P., Takahashi, Y., Xu, X., et al. (2019). Generation of functional lungs via conditional blastocyst complementation using pluripotent stem cells. Nature Medicine *25*, 1691–1698.

34. Regalado, S.G., Qiu, C., Kottapalli, S., Martin, B.K., Chen, W., Liao, H., Kim, H., Li, X., Lalanne, J.-B., Hamazaki, N., et al. (2025). Lineage recording in monoclonal gastruloids reveals heritable modes of early development. bioRxiv. https://doi.org/10.1101/2025.05.23.655664.

35. Canham, M.A., Sharov, A.A., Ko, M.S.H., and Brickman, J.M. (2010). Functional heterogeneity of embryonic stem cells revealed through translational amplification of an early endodermal transcript. PLoS Biol. *8*, e1000379.

36. Kolodziejczyk, A.A., Kim, J.K., Tsang, J.C.H., Ilicic, T., Henriksson, J., Natarajan, K.N., Tuck, A.C., Gao, X., Bühler, M., Liu, P., et al. (2015). Single Cell RNA-Sequencing of Pluripotent States Unlocks Modular Transcriptional Variation. Cell Stem Cell *17*, 471–485.

37. Messmer, T., von Meyenn, F., Savino, A., Santos, F., Mohammed, H., Lun, A.T.L., Marioni, J.C., and Reik, W. (2019). Transcriptional Heterogeneity in Naive and Primed Human Pluripotent Stem Cells at Single-Cell Resolution. Cell Rep *26*, 815–824.e4.

38. Nair, G., Abranches, E., Guedes, A.M.V., Henrique, D., and Raj, A. (2015). Heterogeneous lineage marker expression in naive embryonic stem cells is mostly due to spontaneous differentiation. Sci Rep *5*, 13339.

39. Abranches, E., Guedes, A.M.V., Moravec, M., Maamar, H., Svoboda, P., Raj, A., and Henrique, D. (2014). Stochastic NANOG fluctuations allow mouse embryonic stem cells to explore pluripotency. Development *141*, 2770–2779.

40. Cermola, F., D'Aniello, C., Tatè, R., De Cesare, D., Martinez-Arias, A., Minchiotti, G., and

Patriarca, E.J. (2021). Gastruloid Development Competence Discriminates Different States of Pluripotency. Stem Cell Reports *16*, 354–369.

41. McNamara, H.M., Solley, S.C., Adamson, B., Chan, M.M., and Toettcher, J.E. (2024). Recording morphogen signals reveals mechanisms underlying gastruloid symmetry breaking. Nat Cell Biol *26*, 1832–1844.

42. Moris, N., Anlas, K., van den Brink, S.C., Alemany, A., Schröder, J., Ghimire, S., Balayo, T., van Oudenaarden, A., and Martinez Arias, A. (2020). An in vitro model of early anteroposterior organization during human development. Nature *582*, 410–415.

43. de Jong, M.A., Adegeest, E., Bérenger-Currias, N.M.L.P., Mircea, M., Merks, R.M.H., and Semrau, S. (2024). The shapes of elongating gastruloids are consistent with convergent extension driven by a combination of active cell crawling and differential adhesion. PLoS Comput. Biol. *20*, e1011825.

44. Martin, B.L., and Kimelman, D. (2010). Brachyury establishes the embryonic mesodermal progenitor niche. Genes & Development *24*, 2778.

45. Pijuan-Sala, B., Griffiths, J.A., Guibentif, C., Hiscock, T.W., Jawaid, W., Calero-Nieto, F.J., Mulas, C., Ibarra-Soria, X., Tyser, R.C.V., Ho, D.L.L., et al. (2019). A single-cell molecular map of mouse gastrulation and early organogenesis. Nature *566*, 490–495.

46. Eng, C.-H.L., Lawson, M., Zhu, Q., Dries, R., Koulena, N., Takei, Y., Yun, J., Cronin, C., Karp, C., Yuan, G.-C., et al. (2019). Transcriptome-scale super-resolved imaging in tissues by RNA seqFISH+. Nature *568*, 235–239.

47. Rosen, L.U., Carine Stapel, L., Argelaguet, R., Barker, C.G., Yang, A., Reik, W., and Marioni, J.C. (2022). Inter-gastruloid heterogeneity revealed by single cell transcriptomics time course: implications for organoid based perturbation studies. bioRxiv, 2022.09.27.509783. https://doi.org/10.1101/2022.09.27.509783.

48. Stavish, D., Böiers, C., Price, C., Frith, T.J.R., Halliwell, J., Saldaña-Guerrero, I., Wray, J., Brown, J., Carr, J., James, C., et al. (2020). Generation and trapping of a mesoderm biased state of human pluripotency. Nature Communications *11*, 1–16.

49. Zhou, X., Smith, A.J.H., Waterhouse, A., Blin, G., Malaguti, M., Lin, C.-Y., Osorno, R., Chambers, I., and Lowell, S. (2013). Hes1 desynchronizes differentiation of pluripotent cells by modulating STAT3 activity. Stem Cells *31*, 1511–1522.

50. Kobayashi, T., Mizuno, H., Imayoshi, I., Furusawa, C., Shirahige, K., and Kageyama, R. (2009). The cyclic gene Hes1 contributes to diverse differentiation responses of embryonic stem cells. Genes Dev *23*, 1870–1875.

51. Gery, S., Park, D.J., Vuong, P.T., Chih, D.Y., Lemp, N., and Koeffler, H.P. (2004). Retinoic acid regulates C/EBP homologous protein expression (CHOP), which negatively regulates myeloid target genes. Blood *104*, 3911–3917.

52. Hu, Z.-L., Shi, M., Huang, Y., Zheng, M.-H., Pei, Z., Chen, J.-Y., Han, H., and Ding, Y.-Q. (2011). The role of the transcription factor Rbpj in the development of dorsal root ganglia. Neural Dev *6*, 14.

53. Souilhol, C., Perea-Gomez, A., Camus, A., Beck-Cormier, S., Vandormael-Pournin, S., Escande, M., Collignon, J., and Cohen-Tannoudji, M. (2015). NOTCH activation interferes with cell fate specification in the gastrulating mouse embryo. Development *142*, 3649–3660.

54. Kuwahara, A., Sakai, H., Xu, Y., Itoh, Y., Hirabayashi, Y., and Gotoh, Y. (2014). Tcf3

represses Wnt-β-catenin signaling and maintains neural stem cell population during neocortical development. PLoS One *9*, e94408.

55. Kim, C.H., Oda, T., Itoh, M., Jiang, D., Artinger, K.B., Chandrasekharappa, S.C., Driever, W., and Chitnis, A.B. (2000). Repressor activity of Headless/Tcf3 is essential for vertebrate head formation. Nature *407*, 913–916.

56. Website https://www.biorxiv.org/content/10.1101/2024.12.12.628151v2.full.

57. Latres, E., Chiaur, D.S., and Pagano, M. (1999). The human F box protein beta-Trcp associates with the Cul1/Skp1 complex and regulates the stability of beta-catenin. Oncogene *18*, 849–854.

58. Amel, A., Rabeling, A., Rossouw, S., and Goolam, M. (2023). Wnt and BMP signalling direct anterior–posterior differentiation in aggregates of mouse embryonic stem cells. Biol Open *12*, bio059981.

59. Hennessy, M.J., Fulton, T., Turner, D.A., and Steventon, B. (2023). Negative feedback on Retinoic Acid by Brachyury guides gastruloid symmetry-breaking. bioRxiv, 2023.06.02.543388. https://doi.org/10.1101/2023.06.02.543388.

60. Dias, A., Pascual-Mas, P., Robertson, G., Torregrosa-Cortés, G., Stelloo, S., Casaní-Galdón, P., Babin, S., Romaniuk, Y., Mayran, A., Wehmeyer, A.E., et al. (2025). Opposing Nodal and Wnt signalling activities govern the emergence of the mammalian body plan. bioRxiv, 2025.01.11.632562. https://doi.org/10.1101/2025.01.11.632562.

61. Underhill, E.J., and Toettcher, J.E. (2023). Control of gastruloid patterning and morphogenesis by the Erk and Akt signaling pathways. Development *150*. https://doi.org/10.1242/dev.201663.

62. Suppinger, S., Zinner, M., Aizarani, N., Lukonin, I., Ortiz, R., Azzi, C., Stadler, M.B., Vianello, S., Palla, G., Kohler, H., et al. (2023). Multimodal characterization of murine gastruloid development. Cell Stem Cell *30*, 867–884.e11.

63. Weber, T.S., Biben, C., Miles, D.C., Glaser, S.P., Tomei, S., Lin, C.-Y., Kueh, A., Pal, M., Zhang, S., Tam, P.P.L., et al. (2025). LoxCode in vivo barcoding reveals epiblast clonal fate bias to fetal organs. Cell. https://doi.org/10.1016/j.cell.2025.04.026.

64. Peng, G., Suo, S., Chen, J., Chen, W., Liu, C., Yu, F., Wang, R., Chen, S., Sun, N., Cui, G., et al. (2020). Spatial Transcriptome for the Molecular Annotation of Lineage Fates and Cell Identity in Mid-gastrula Mouse Embryo. Dev Cell *55*, 802–804.

65. Mohammed, H., Hernando-Herraez, I., Savino, A., Scialdone, A., Macaulay, I., Mulas, C., Chandra, T., Voet, T., Dean, W., Nichols, J., et al. (2017). Single-Cell Landscape of Transcriptional Heterogeneity and Cell Fate Decisions during Mouse Early Gastrulation. Cell Rep *20*, 1215–1228.

66. Wehmeyer, A.E., Schmitt, J.K., Eggersdorfer, F., Zissel, L., Schröder, C.M., Tekman, M., Dias, A., Schüle, K.M., Probst, S., Martinez-Arias, A., et al. (2025). Competing regulatory modules control the transition between mammalian gastrulation modes. bioRxiv, 2025.05.07.652670. https://doi.org/10.1101/2025.05.07.652670.

67. Regalado, S.G., Qiu, C., Lalanne, J.-B., Martin, B.K., Duran, M., Trapnell, C., Keith, A., Domcke, S., and Shendure, J. (2025). Barcoded monoclonal embryoids are a potential solution to confounding bottlenecks in mosaic organoid screens. bioRxiv, 2025.05.23.655669. https://doi.org/10.1101/2025.05.23.655669.

68. Bowling, S., Di Gregorio, A., Sancho, M., Pozzi, S., Aarts, M., Signore, M., D Schneider, M., Martinez-Barbera, J.P., Gil, J., and Rodríguez, T.A. (2018). P53 and mTOR signalling determine fitness selection through cell competition during early mouse embryonic development. Nat Commun *9*, 1763.

69. Braccioli, L., van den Brand, T., Alonso Saiz, N., Fountas, C., Celie, P.H.N., Kazokaitė-Adomaitienė, J., and de Wit, E. (2025). Identifying cross-lineage dependencies of cell-type-specific regulators in mouse gastruloids. Dev Cell. https://doi.org/10.1016/j.devcel.2025.02.013.

70. Blastocyst complementation-based rat-derived heart generation reveals cardiac anomaly barriers to interspecies chimera development (2024). iScience *27*, 111414.

71. Ruiz-Estevez, M., Crane, A.T., Rodriguez-Villamil, P., Ongaratto, F.L., You, Y., Steevens, A.R., Hill, C., Goldsmith, T., Webster, D.A., Sherry, L., et al. (2021). Liver development is restored by blastocyst complementation of HHEX knockout in mice and pigs. Stem Cell Research & Therapy *12*, 1–13.

72. Esmaeili, A., Eteghadi, A., Landi, F.S., Yavari, S.F., and Taghipour, N. (2024). Recent approaches in regenerative medicine in the fight against neurodegenerative disease. Brain Res *1825*, 148688.

73. Mao, J., Saiding, Q., Qian, S., Liu, Z., Zhao, B., Zhao, Q., Lu, B., Mao, X., Zhang, L., Zhang, Y., et al. (2022). Reprogramming stem cells in regenerative medicine. Smart Medicine *1*, e20220005.

74. Moriwaki, T., Tani, H., Haga, K., Morita-Umei, Y., Soma, Y., Umei, T.C., Sekine, O., Takatsuna, K., Kishino, Y., Kanazawa, H., et al. (2023). Scalable production of homogeneous cardiac organoids derived from human pluripotent stem cells. Cell Rep Methods *3*, 100666.

75. Cai, D., Cohen, K.B., Luo, T., Lichtman, J.W., and Sanes, J.R. (2013). Improved tools for the Brainbow toolbox. Nat. Methods *10*, 540–547.

76. Stringer, C., and Pachitariu, M. (2025). Cellpose3: one-click image restoration for improved cellular segmentation. Nat Methods *22*, 592–599.

77. Stringer, C., Wang, T., Michaelos, M., and Pachitariu, M. (2021). Cellpose: a generalist algorithm for cellular segmentation. Nat Methods *18*, 100–106.

78. Comparable Generation of Activin-Induced Definitive Endoderm via Additive Wnt or BMP Signaling in Absence of Serum (2014). Stem Cell Reports *3*, 5–14.

79. Corces, M.R., Trevino, A.E., Hamilton, E.G., Greenside, P.G., Sinnott-Armstrong, N.A., Vesuna, S., Satpathy, A.T., Rubin, A.J., Montine, K.S., Wu, B., et al. (2017). An improved ATAC-seq protocol reduces background and enables interrogation of frozen tissues. Nat Methods *14*, 959–962.

80. Wang, Q., Li, M., Wu, T., Zhan, L., Li, L., Chen, M., Xie, W., Xie, Z., Hu, E., Xu, S., et al. (2022). Exploring Epigenomic Datasets by ChIPseeker. Curr Protoc *2*, e585.

81. Heinz, S., Benner, C., Spann, N., Bertolino, E., Lin, Y.C., Laslo, P., Cheng, J.X., Murre, C., Singh, H., and Glass, C.K. (2010). Simple combinations of lineage-determining transcription factors prime cis-regulatory elements required for macrophage and B cell identities. Mol. Cell *38*, 576–589.

82. van der Walt, S., Schönberger, J.L., Nunez-Iglesias, J., Boulogne, F., Warner, J.D., Yager,

N., Gouillart, E., Yu, T., and scikit-image contributors (2014). scikit-image: image processing in Python. PeerJ *2*, e453.

Figure 1

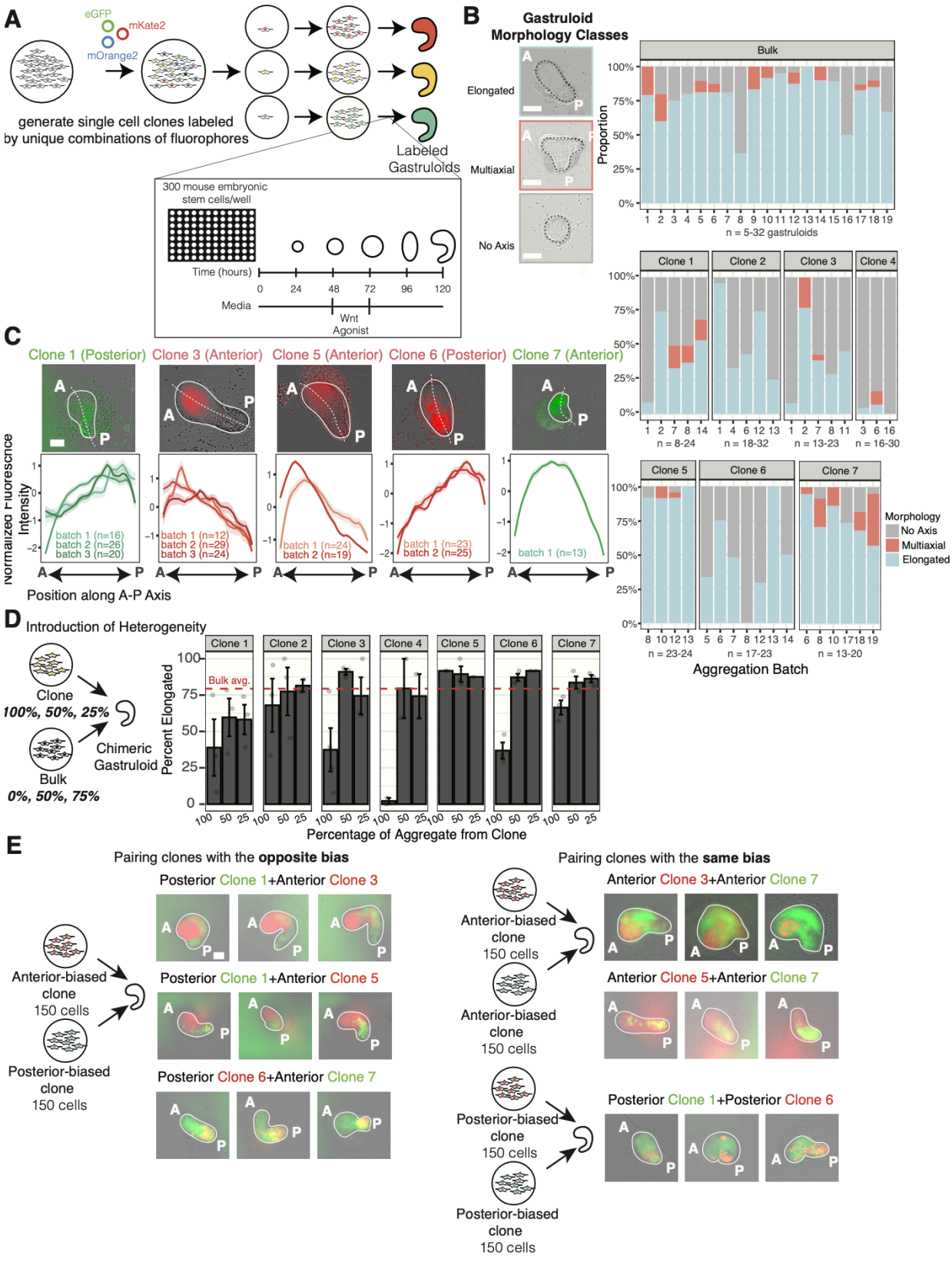
A
eGFP
mKate2
mOrange2
generate single cell clones labeled by unique combinations of fluorophores
Labeled Gastruloids
300 mouse embryonic stem cells/well
Time (hours)
0 24 48 72 96 120
Media
Wnt Agonist
B
Gastruloid Morphology Classes
Elongated
Multiaxial
No Axis
Bulk
Proportion
n = 5-32 gastruloids
Clone 1
Clone 2
Clone 3
Clone 4
n = 8-24
n = 18-32
n = 13-23
n = 16-30
Clone 5
Clone 6
Clone 7
n = 23-24
n = 17-23
n = 13-20
Aggregation Batch
Morphology
No Axis
Multiaxial
Elongated
C
Clone 1 (Posterior)
Clone 3 (Anterior)
Clone 5 (Anterior)
Clone 6 (Posterior)
Clone 7 (Anterior)
Normalized Fluorescence Intensity
batch 1 (n=16)
batch 2 (n=26)
batch 3 (n=20)
batch 1 (n=12)
batch 2 (n=29)
batch 3 (n=24)
batch 1 (n=24)
batch 2 (n=19)
batch 1 (n=23)
batch 2 (n=25)
batch 1 (n=13)
Position along A-P Axis
D
Introduction of Heterogeneity
Clone
100%, 50%, 25%
Bulk
0%, 50%, 75%
Chimeric Gastruloid
Percent Elongated
Bulk avg.
Percentage of Aggregate from Clone
E
Pairing clones with the opposite bias
Anterior-biased clone 150 cells
Posterior-biased clone 150 cells
Posterior Clone 1+Anterior Clone 3
Posterior Clone 1+Anterior Clone 5
Posterior Clone 6+Anterior Clone 7
Pairing clones with the same bias
Anterior-biased clone 150 cells
Anterior Clone 3+Anterior Clone 7
Anterior Clone 5+Anterior Clone 7
Posterior-biased clone 150 cells
Posterior Clone 1+Posterior Clone 6

Figure 2

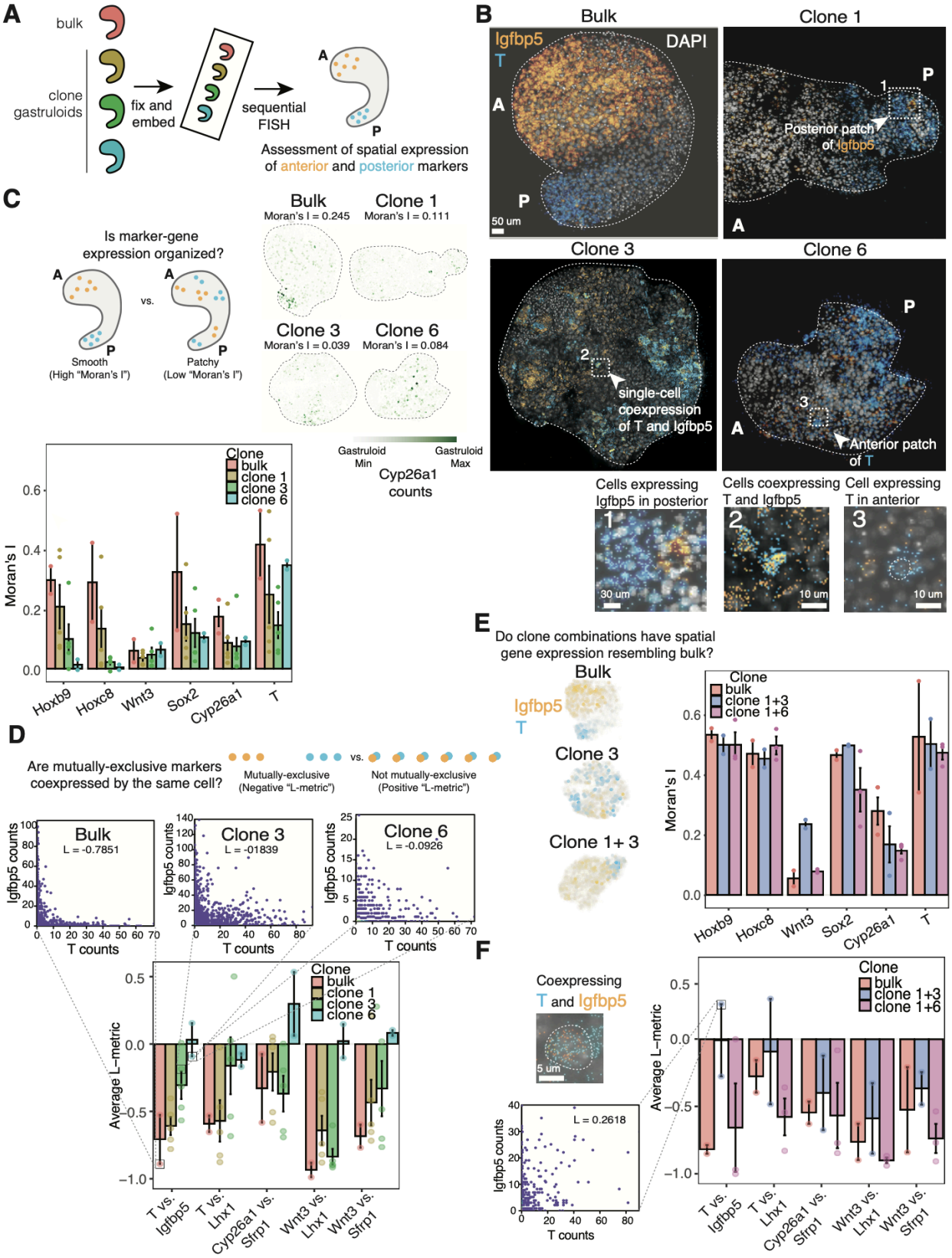
A
bulk
clone gastruloids
fix and embed
sequential FISH
Assessment of spatial expression of anterior and posterior markers
B
Bulk
Clone 1
Clone 3
Clone 6
Igfbp5
T
DAPI
50 um
Posterior patch of Igfbp5
single-cell coexpression of T and Igfbp5
Anterior patch of T
Cells expressing Igfbp5 in posterior
Cells coexpressing T and Igfbp5
Cell expressing T in anterior
30 um
10 um
C
Is marker-gene expression organized?
Smooth (High "Moran's I")
Patchy (Low "Moran's I")
Moran's I = 0.245
Moran's I = 0.111
Moran's I = 0.039
Moran's I = 0.084
Gastruloid Min
Gastruloid Max
Cyp26a1 counts
Clone
bulk
clone 1
clone 3
clone 6
Moran's I
Hoxb9
Hoxc8
Wnt3
Sox2
Cyp26a1
T
D
Are mutually-exclusive markers coexpressed by the same cell?
Mutually-exclusive (Negative "L-metric")
Not mutually-exclusive (Positive "L-metric")
L = -0.7851
L = -01839
L = -0.0926
Igfbp5 counts
T counts
Average L-metric
T vs. Igfbp5
T vs. Lhx1
Cyp26a1 vs. Sfrp1
Wnt3 vs. Lhx1
Wnt3 vs. Sfrp1
E
Do clone combinations have spatial gene expression resembling bulk?
Clone 1+ 3
clone 1+3
clone 1+6
F
Coexpressing T and Igfbp5
5 um
L = 0.2618

Figure 3

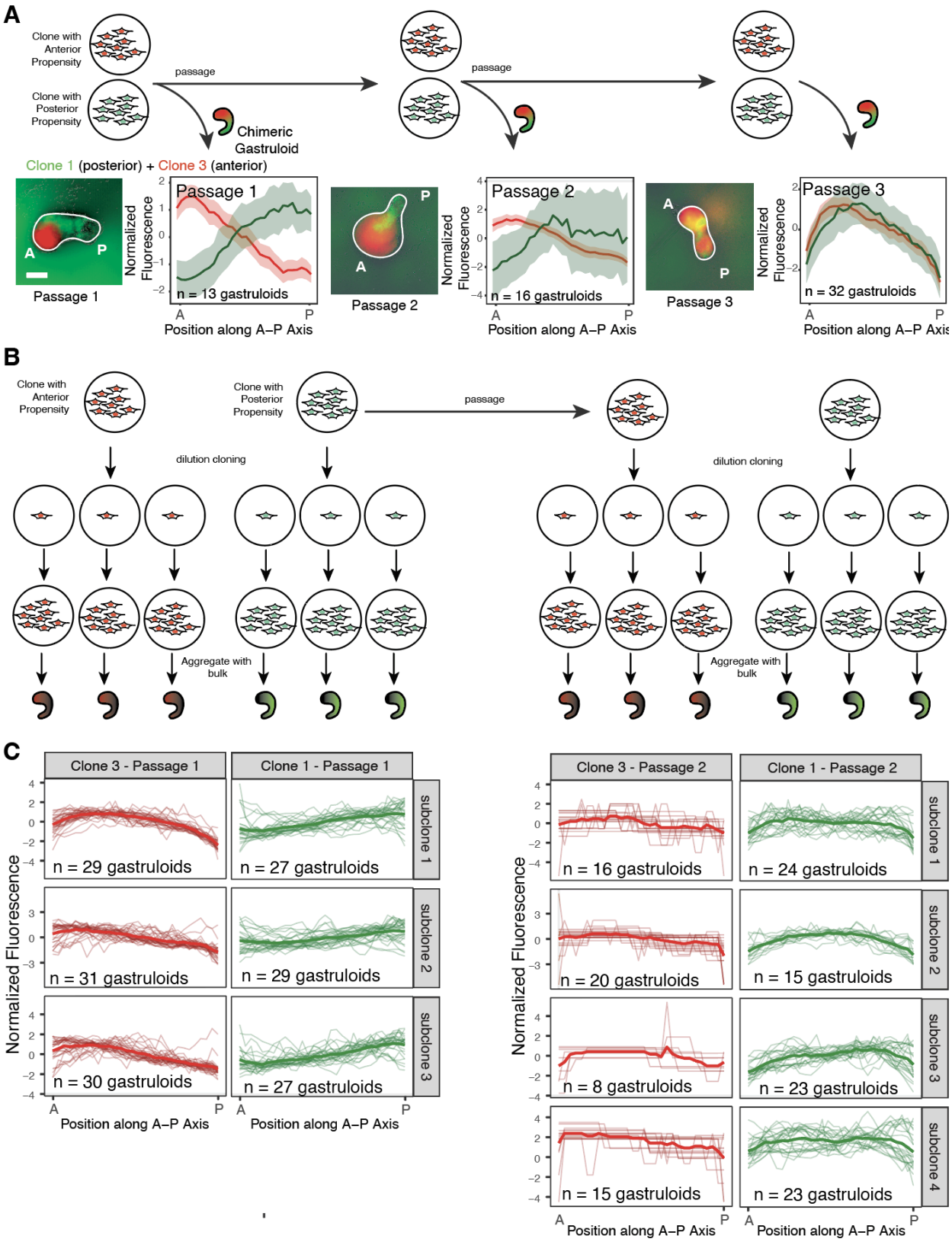
A
Clone with Anterior Propensity
Clone with Posterior Propensity
passage
Chimeric Gastruloid
Clone 1 (posterior) + Clone 3 (anterior)
Passage 1
Normalized Fluorescence
n = 13 gastruloids
Position along A–P Axis
Passage 2
n = 16 gastruloids
Passage 3
n = 32 gastruloids
B
dilution cloning
Aggregate with bulk
C
Clone 3 - Passage 1
Clone 1 - Passage 1
Clone 3 - Passage 2
Clone 1 - Passage 2
subclone 1
subclone 2
subclone 3
subclone 4
n = 29 gastruloids
n = 27 gastruloids
n = 31 gastruloids
n = 29 gastruloids
n = 30 gastruloids
n = 27 gastruloids
n = 16 gastruloids
n = 24 gastruloids
n = 20 gastruloids
n = 15 gastruloids
n = 8 gastruloids
n = 23 gastruloids
n = 15 gastruloids
n = 23 gastruloids

Figure 4

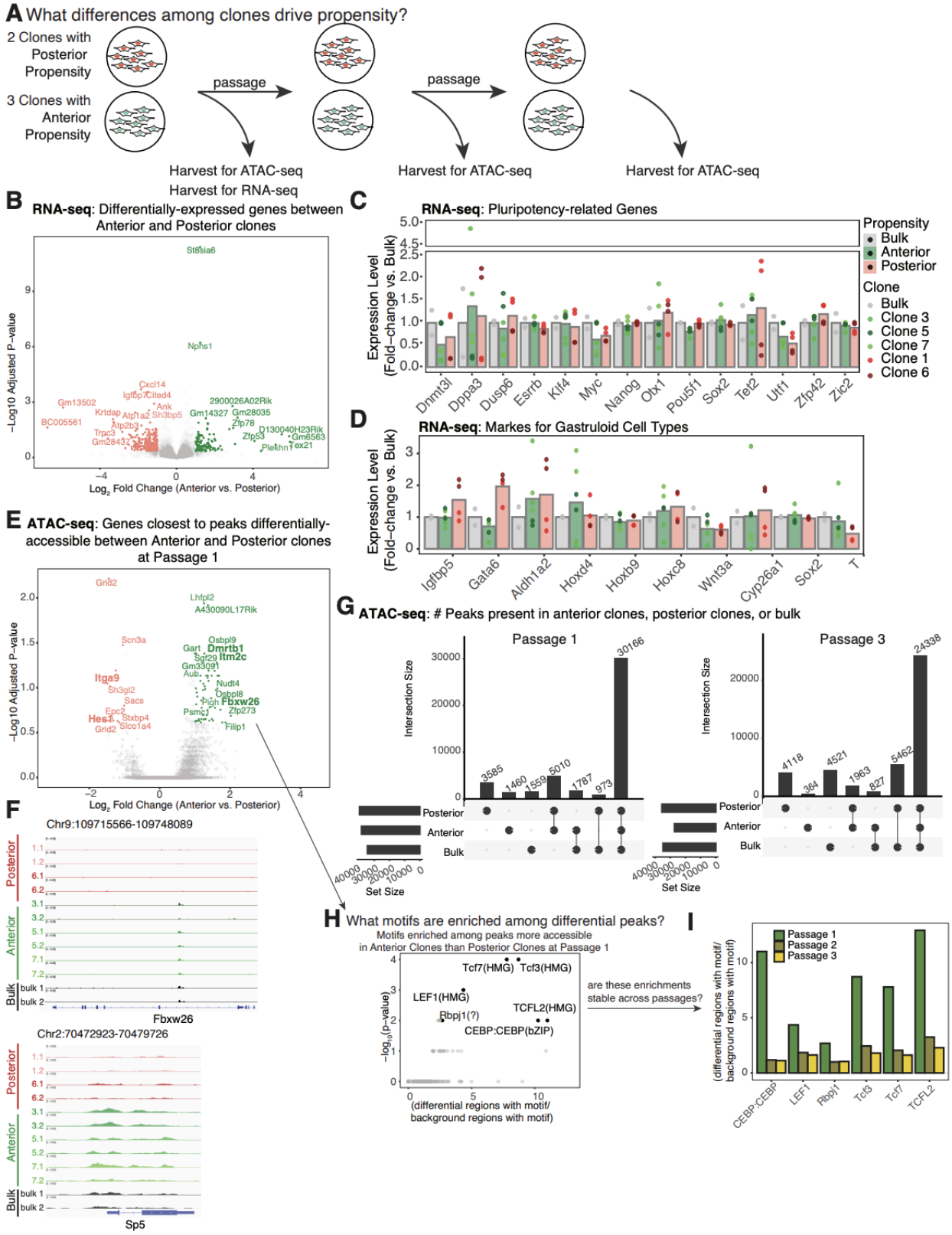
A What differences among clones drive propensity?
2 Clones with Posterior Propensity
3 Clones with Anterior Propensity
passage
passage
Harvest for ATAC-seq
Harvest for RNA-seq
Harvest for ATAC-seq
Harvest for ATAC-seq
B RNA-seq: Differentially-expressed genes between Anterior and Posterior clones
−Log10 Adjusted P-value
Log2 Fold Change (Anterior vs. Posterior)
C RNA-seq: Pluripotency-related Genes
Expression Level (Fold-change vs. Bulk)
Propensity
Bulk
Anterior
Posterior
Clone
Bulk
Clone 3
Clone 5
Clone 7
Clone 1
Clone 6
Dnmt3l
Dppa3
Dusp6
Esrrb
Klf4
Myc
Nanog
Otx1
Pou5f1
Sox2
Tet2
Utf1
Zfp42
Zic2
D RNA-seq: Markes for Gastruloid Cell Types
Expression Level (Fold-change vs. Bulk)
Igfbp5
Gata6
Aldh1a2
Hoxd4
Hoxb9
Hoxc8
Wnt3a
Cyp26a1
Sox2
T
E ATAC-seq: Genes closest to peaks differentially-accessible between Anterior and Posterior clones at Passage 1
−Log10 Adjusted P-value
Log2 Fold Change (Anterior vs. Posterior)
F
Chr9:109715566-109748089
Posterior
Anterior
Bulk
Fbxw26
Chr2:70472923-70479726
Sp5
G ATAC-seq: # Peaks present in anterior clones, posterior clones, or bulk
Passage 1
Passage 3
Intersection Size
Set Size
Posterior
Anterior
Bulk
H What motifs are enriched among differential peaks?
Motifs enriched among peaks more accessible in Anterior Clones than Posterior Clones at Passage 1
Tcf7(HMG)
Tcf3(HMG)
LEF1(HMG)
Rbpj1(?)
TCFL2(HMG)
CEBP:CEBP(bZIP)
−log10(p-value)
(differential regions with motif/ background regions with motif)
are these enrichments stable across passages?
I
Passage 1
Passage 2
Passage 3
(differential regions with motif/ background regions with motif)
CEBP:CEBP
LEF1
Rbpj1
Tcf3
Tcf7
TCFL2

Figure 5

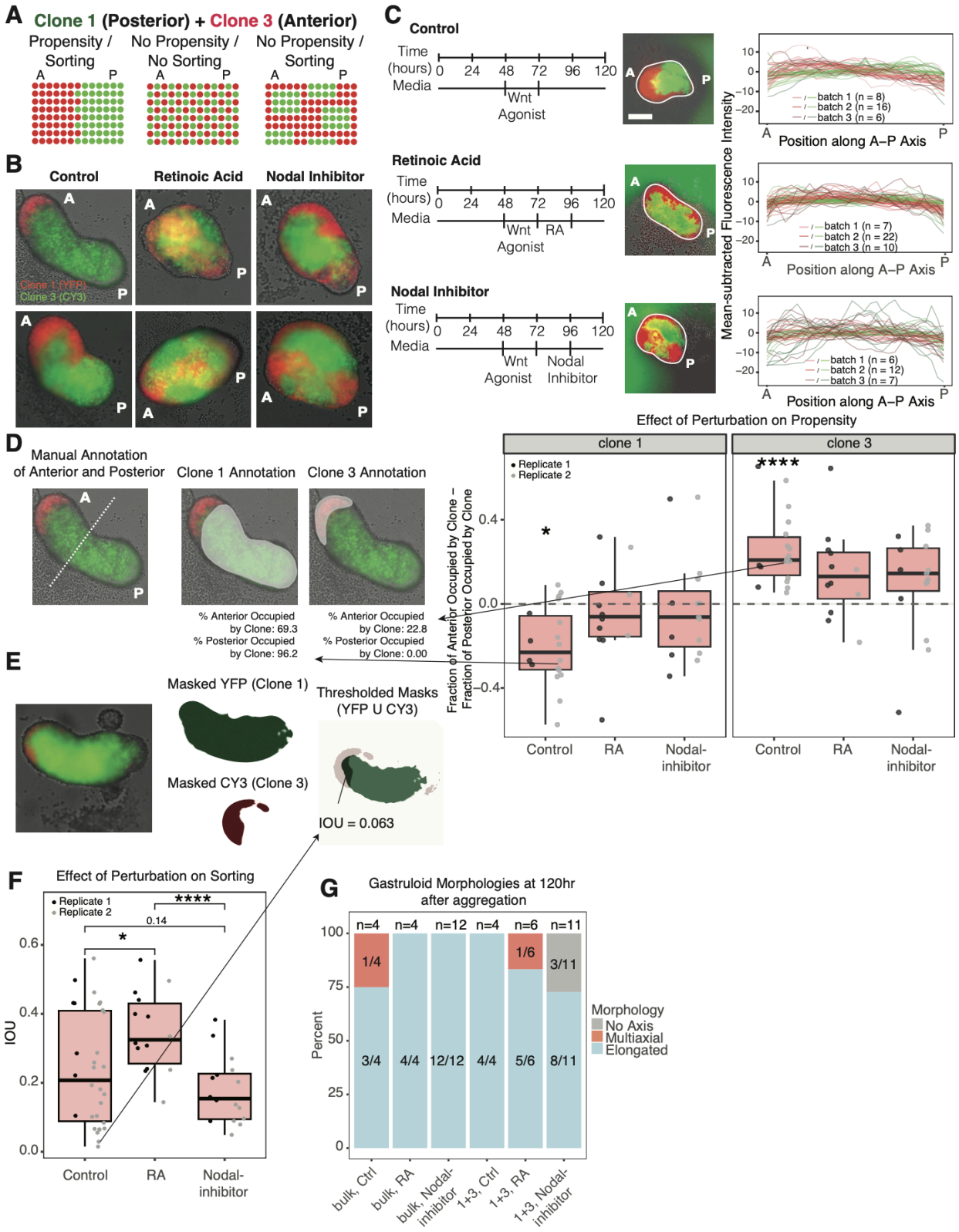
A
Clone 1 (Posterior) + Clone 3 (Anterior)
Propensity / Sorting
No Propensity / No Sorting
No Propensity / Sorting
B
Control
Retinoic Acid
Nodal Inhibitor
Clone 1 (YFP)
Clone 3 (CY3)
C
Control
Time (hours) 0 24 48 72 96 120
Media
Wnt Agonist
Retinoic Acid
Wnt Agonist RA
Nodal Inhibitor
Wnt Agonist Nodal Inhibitor
Mean-subtracted Fluorescence Intensity
batch 1 (n = 8)
batch 2 (n = 16)
batch 3 (n = 6)
batch 1 (n = 7)
batch 2 (n = 22)
batch 3 (n = 10)
batch 1 (n = 6)
batch 2 (n = 12)
batch 3 (n = 7)
Position along A–P Axis
D
Manual Annotation of Anterior and Posterior
Clone 1 Annotation
Clone 3 Annotation
% Anterior Occupied by Clone: 69.3
% Posterior Occupied by Clone: 96.2
% Anterior Occupied by Clone: 22.8
% Posterior Occupied by Clone: 0.00
Effect of Perturbation on Propensity
clone 1
clone 3
Replicate 1
Replicate 2
Fraction of Anterior Occupied by Clone – Fraction of Posterior Occupied by Clone
Control
RA
Nodal-inhibitor
E
Masked YFP (Clone 1)
Masked CY3 (Clone 3)
Thresholded Masks (YFP U CY3)
IOU = 0.063
F
Effect of Perturbation on Sorting
Replicate 1
Replicate 2
0.14
IOU
Control
RA
Nodal-inhibitor
G
Gastruloid Morphologies at 120hr after aggregation
n=4 n=4 n=12 n=4 n=6 n=11
1/4
3/4
4/4
12/12
4/4
1/6
5/6
3/11
8/11
Percent
Morphology
No Axis
Multiaxial
Elongated
bulk, Ctrl
bulk, RA
bulk, Nodal-inhibitor
1+3, Ctrl
1+3, RA
1+3, Nodal-inhibitor

Figure 6

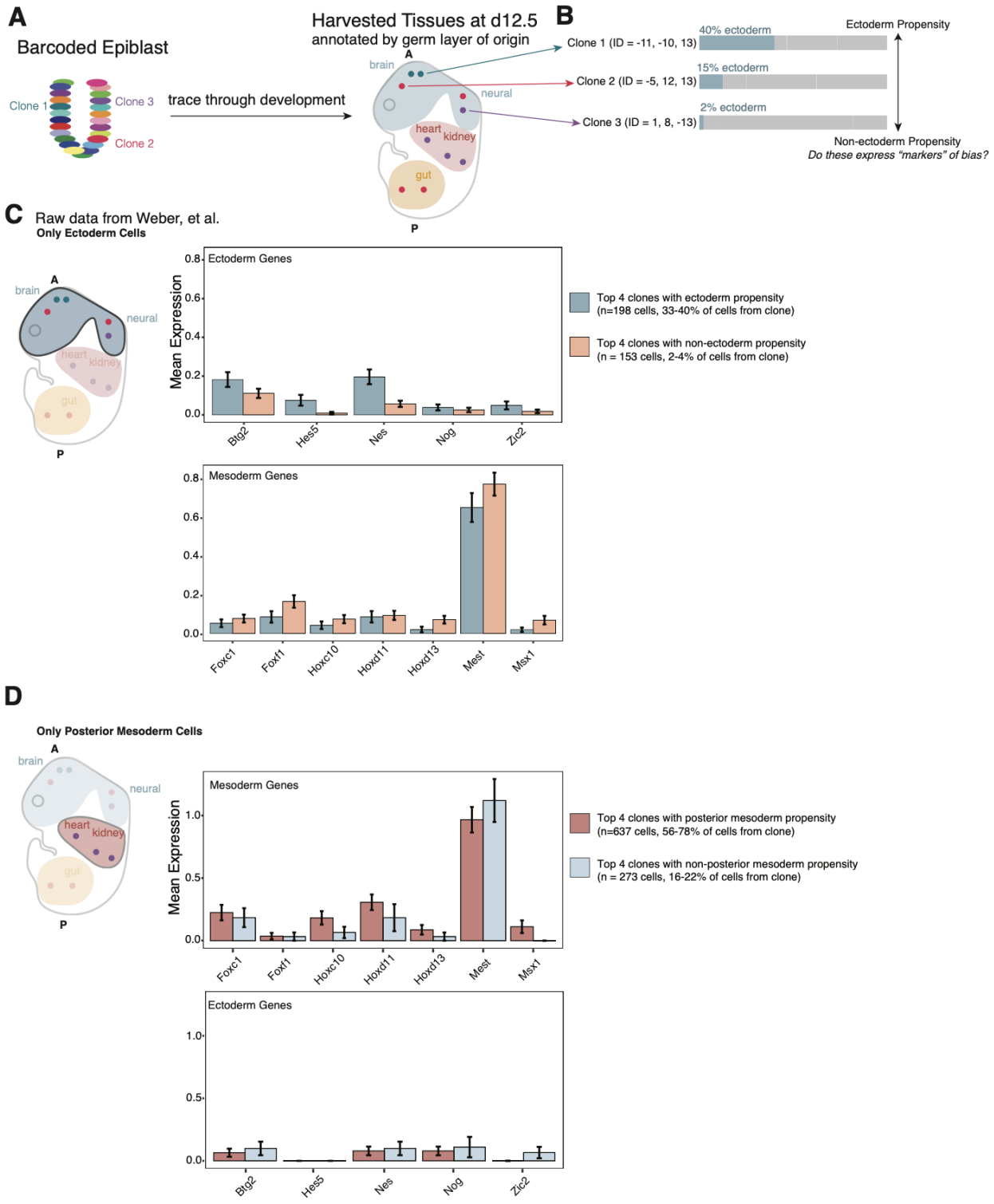
A
Barcoded Epiblast
Clone 1
Clone 3
Clone 2
trace through development
Harvested Tissues at d12.5
annotated by germ layer of origin
A
brain
neural
heart
kidney
gut
P
B
Clone 1 (ID = -11, -10, 13)
40% ectoderm
Clone 2 (ID = -5, 12, 13)
15% ectoderm
Clone 3 (ID = 1, 8, -13)
2% ectoderm
Ectoderm Propensity
Non-ectoderm Propensity
Do these express "markers" of bias?
C
Raw data from Weber, et al.
Only Ectoderm Cells
Ectoderm Genes
Mean Expression
Top 4 clones with ectoderm propensity
(n=198 cells, 33-40% of cells from clone)
Top 4 clones with non-ectoderm propensity
(n = 153 cells, 2-4% of cells from clone)
Btg2
Hes5
Nes
Nog
Zic2
Mesoderm Genes
Foxc1
Foxf1
Hoxc10
Hoxd11
Hoxd13
Mest
Msx1
D
Only Posterior Mesoderm Cells
Mesoderm Genes
Mean Expression
Top 4 clones with posterior mesoderm propensity
(n=637 cells, 56-78% of cells from clone)
Top 4 clones with non-posterior mesoderm propensity
(n = 273 cells, 16-22% of cells from clone)
Ectoderm Genes